THESIS FOR THE DEGREE OF DOCTOR OF PHILOSOPHY

Fiber-optic communications with microresonator frequency combs

ATTILA FÜLÖP

CHALMERS

Photonics Laboratory
Department of Microtechnology and Nanoscience (MC2)
CHALMERS UNIVERSITY OF TECHNOLOGY

Göteborg, Sweden 2018

Fiber-optic communications with microresonator frequency combs
ATTILA FÜLÖP

ISBN 978–91–7597–712–6

Doktorsavhandling vid Chalmers Tekniska Högskola
Ny serie 4393
ISSN 0346–718X

Technical Report MC2–381
ISSN 1652–0769

Photonics Laboratory
Department of Microtechnology and Nanoscience (MC2)
Chalmers University of Technology
SE-412 96 Göteborg, Sweden
Telephone: +46 (0)31-772 1000

Front cover illustration: Sketch showing the lines from a microresonator comb being modulated with data encoded using QPSK, 16QAM and 64QAM.

Printed by Chalmers Reproservice
Göteborg, Sweden 2018

Fiber-optic communications with microresonator frequency combs
Thesis for the degree of Doctor of Philosophy
ATTILA FÜLÖP
Department of Microtechnology and Nanoscience (MC2)
Photonics Laboratory
Chalmers University of Technology

Abstract

Modern data communication links target ever-higher information throughput. To utilize the available bandwidth in a single strand of fiber, optical communication links often require a large number of lasers, each operating at a different wavelength. A microresonator frequency comb is a chip-scale multi-wavelength laser source whose spectrum consists of multiple evenly spaced lines. As the line spacing of a microresonator comb is on the order of several tens of GHz, it provides a promising light source candidate for implementing an integrated multi-wavelength transceiver. The interest for using microresonator combs in communications applications has therefore increased greatly in the last five years. The application-related developments have been complemented with an increased exploration and understanding of the operating principles behind these devices.

This thesis studies microresonator frequency combs in both long-haul and high data-rate (multi-terabit per second) fiber communications systems. The results specifically include the longest demonstrated communications link with a microresonator light source as well as the highest order modulation format demonstration using any integrated comb source. The used microresonators are based on a high-Q silicon nitride platform provided by our collaborators at Purdue University. Part of the results are enabled by the high line powers resulting from a recently demonstrated novel comb state. This state bears similarities with dark solitons in fibers in that it corresponds to a train of dark pulses circulating inside the microresonator cavity. Overall, the results in this thesis provide a promising pathway towards enabling a future chip-scale multi-wavelength coherent transmitter.

Keywords: Fiber-optic communication, integrated optics devices, nonlinear optics, four-wave mixing, microresonators.

Sammanfattning

Moderna kommunikationslänkar designas idag för att stödja allt högre datatakter. För att utnyttja den optiska fiberns tillgängliga bandbredd används i dagsläget därför ofta flera lasrar med olika våglängder parallellt. En mikroresonatorbaserad frekvenskam är en ljuskälla som får plats på en integrerad krets som kan avge flera jämnt åtskilda våglängder samtidigt. I och med att linjerna skiljs åt med flera tiotals GHz skulle en sådan krets kunna möjliggöra en komplett integrerad flerkanalssändare. Intresset för mikroresonatorer i kommunikationssammanhang har därför ökat markant de senaste fem åren. Applikationsnära forskning har även kompletterats med ökad forskning kring hur dessa enheter fungerar och kan optimeras.

Den här avhandlingen beskriver och utvärderar mikroresonatorer för kommunikationstillämpningar för både lång-distanslänkar och länkar med hög datatakt (dvs. flera terabit per sekund). De inkluderade resultaten beskriver den längsta demonstrerade länken där mikroresonatorer använts samt en demonstration med den hittills högsta ordningens modulationsformat som använts med någon integrerad kamkälla. Våra mikroresonatorer är baserade på en hög-Q kiselnitridplattform som tillverkats av våra samarbetspartners på Purdue University i USA. Delar av resultaten har möjliggjorts av de höga linjeeffekterna som en nyligen upptäckt kamtyp genererade. Denna kamtyp liknar mörka solitoner i klassiska fibersystem i att den motsvaras av en cirkulerande mörk puls i resonatorkaviteten. Sammanfattningsvis pekar resultaten i avhandlingen ut en lovande riktning för att möjliggöra framtida integrerade flerkanaliga koherenta optiska sändare.

Kivonat

Modern kommunikációs rendszerek egyre magasabb adatsebességeket céloznak meg. Az optikai üvegszál sávszélességének maximális kihasználásáért ezért manapság gyakran több különböző hullámhosszú lézert használnak az adóvevőkben. Egy mikrorezonátor-alapú frekvenciafésű egy olyan integrált áramkör-nagyságú fényforrás, amely egyszerre több különböző frekvenciájú fényt ad ki. Mivel a vonalak több tíz GHz szórással egyenletesen vannak elosztva, egy mikrorezotátor fésű igéretes fényforrásnak tűnik egy több-csatornájú integrált adóvevőhöz. Emiatt, a kommunikációhoz alkalmas mikrorezonátorok felé irányuló érdeklődés az utóbbi öt évben nagy mértékben megnőtt. Az alkalmazásokra fókuszáló kutatás mellett, az egységek működésének elmélete iránti kutatás is gyorsan fejlődik.

Ez a dolgozat a mikrorezonátorok nagytávolságú és magas adatmennyiségű (több mint egy pár terabit per másodperc) kommunikációs alkalmazásáról szól. A bemutatott eredmények között említendő az eddigi leghosszabb távolságon működő mikrorezonátor-alapú kommunikációs rendszer. Ezenkívűl, a csatolt cikkekben bemutatjuk azt a kisérleti rendszert, amelyben integrált frekvenciafésűkre eddig elért legmagasabb rendű modulációt megvalósítottuk. A mikrorezonátorainkat a Purdue Universityn dolgozó partnereik állították elő magas-Q szilicium-nitrid alapú platformon. Az eredmények egy részét egy újonnan kifejlesztett fésűtípús magas energiájú vonalai tettek lehetővé. Ez a típusú fésű a klasszikus üvegszálakban terjedő sötét szolitonhoz hasonlóan, a rezonátorban keringő sötét pulzusoknak felel meg. Végül, a dolgozatban bemutatott eredmények a jövőbeli integrált többcsatornájú koherens optikai adóvevők fejlesztésének egy igéretes irányát adják meg.

Acknowledgements

First of all, I would like to thank my supervisor, Associate Prof. Victor Torres-Company, without his continuing active support and knowledge I would not have made it this far. I would additionally also like to thank my examiner Prof. Peter Andrekson for discussions and lab support and Prof. Magnus Karlsson for discussions and teaching of the relevant topics.

I would also like to thank and acknowledge Pei-Hsun Wang, Abdullah Al Noman, Prof. Andrew Weiner and the rest of the ultrafast optics laboratory at Purdue University. I appreciate very much the great support and kindness I received when I visited. Most of the experimental results in this thesis have been possible thanks to you!

Moreover I would like to thank all the members of the photonics laboratory here at Chalmers. Specifically I would like to thank Emanuel Haglund for our friendship during our whole Chalmers education and Clemens Krückel both for great discussions on nonlinear optics and organizing epic out-of office trips. Lars Lundberg and Dr. Tobias Eriksson deserve special thanks for our great roadtrip through death valley and the great metropolis of Beatty! I would like to thank Dr. Erik Haglund and Óskar Bjarki Helgason for being great office mates providing discussions both around and beyond the topics that we are each working on. Additionally I would also like to thank Mikael Mazur and Dr. Abel Lorences-Riesgo for being very helpful and patient in teaching me about the intricacies of the transmission lab and of course the related great discussions! Furthermore, I would like to thank Dr. Krzysztof Szczerba and Dr. Vicente Durán Bosch for the fika-room and after-work discussions brightening many rainy Fridays. I would also like to thank Prof. Enrique Silvestre for our collaboration and for teaching me about waveguide simulations and modelling.

Last, but not least, I would like to thank all of my family and friends for being supportive and great to be around.

List of Papers

This thesis is based on the following appended papers:

[A] **A. Fülöp**, M. Mazur, A. Lorences-Riesgo, T. A. Eriksson, P.-H. Wang, Y. Xuan, D. E. Leaird, M. Qi, P. A. Andrekson, A. M. Weiner, and V. Torres-Company, "Long-haul coherent communications using microresonator frequency combs", *Optics Express*, vol. 25, no. 22, pp. 26678–26688, 2017.

[B] **A. Fülöp**, M. Mazur, A. Lorences-Riesgo, P.-H. Wang, Y. Xuan, D. E. Leaird, M. Qi, P. A. Andrekson, A. M. Weiner, and V. Torres-Company, "Frequency noise of a normal dispersion microresonator-based frequency comb", *Optical Fiber Communications conference (OFC)*, Los Angeles, USA, paper W2A.6, 2017.

[C] **A. Fülöp**, P.-H. Wang, Y. Xuan, D. E. Leaird, M. Qi, P. A. Andrekson, A. M. Weiner, and V Torres-Company, "Active feedback stabilization of normal-dispersion microresonator combs", *European conference on Lasers and Electro-optics (CLEO Europe)*, Munich, Germany, paper CD-P-45, 2017.

[D] **A. Fülöp**, M. Mazur, A. Lorences-Riesgo, Ó. B. Helgason, P.-H. Wang, Y. Xuan, D. E. Leaird, M. Qi, P. A. Andrekson, A. M. Weiner, and V. Torres-Company, "High-order coherent communications using mode-locked dark pulse Kerr combs from microresonators", *Under review*, 2017.

[E] **A. Fülöp**, C. J. Krückel, D. Castelló-Lurbe, E. Silvestre, and V. Torres-Company, "Triply resonant coherent four-wave mixing in silicon nitride microresonators", *Optics Letters*, vol. 40, no. 17, pp. 4006–4009, 2015.

Related publications and conference contributions by the author, not included in the thesis:

[F] C. J. Krückel, **A. Fülöp**, P. A. Andrekson, and V. Torres-Company, "Continuous-wave nonlinear optics in low-stress silicon nitride waveguides", *Optical Fiber Communication Conference (OFC)*, Los Angeles, USA, paper W1K.4, 2015.

[G] **A. Fülöp**, C. J. Krückel, D. Castelló-Lurbe, E. Silvestre, and V. Torres-Company, "Phase-sensitive resonant four-wave mixing in silicon nitride microresonators", *Conference on Lasers and Electro-Optics (CLEO) Europe*, Munich, Germany, paper CD_P_9, 2015.

[H] A. Lorences-Riesgo, T. A. Eriksson, **A. Fülöp**, M. Karlsson, and P. A. Andrekson, "Frequency-comb regeneration for self-homodyne superchannels", *European Conference and Exhibition on Cptical Communication (ECOC)*, Valencia, Spain, paper We.3.6.2., 2015.

[I] C. J. Krückel, **A. Fülöp**, T. Klintberg, J. Bengtsson, P. A. Andrekson, and V. Torres-Company, "Linear and nonlinear characterization of low-stress high-confinement silicon-rich nitride waveguides", *Optics Express*, vol. 23, no. 20, pp. 25827–25837, 2015.

[J] A. Lorences-Riesgo, T. A. Eriksson, **A. Fülöp**, P. A. Andrekson, and M. Karlsson, "Frequency-comb regeneration for self-homodyne superchannels", *Journal of Lightwave Technology*, vol. 34, no. 8, pp. 1800–1806, 2016.

[K] M. Rezagholipour Dizaji, C. J. Krückel, **A. Fülöp**, P. A. Andrekson, V. Torres-Company, and L. R. Chen, "Cross-phase-modulation-based wavelength conversion in low-stress silicon-rich nitride waveguide", *Optical Fiber Communication Conference (OFC)*, Anaheim, USA, paper Tu2K.4, 2016.

[L] X. Liu, M. Pu, B. Zhou, C. J. Krückel, **A. Fülöp**, V. Torres-Company, and M. Bache, "Octave-spanning supercontinuum generation in a silicon-rich nitride waveguide", *Optics Letters*, vol. 41, no. 12, pp. 2719–2722, 2016.

[M] X. Liu, M. Pu, B. Zhou, C. J. Krückel, **A. Fülöp**, V. Torres-Company, and M. Bache, "Octave-spanning supercontinuum generation in a silicon-rich nitride waveguide", *Conference on Lasers and Electro-Optics (CLEO)*, San Jose, USA, paper SW1Q.3, 2016.

[N] **A. Fülöp**, M. Mazur, T. A. Eriksson, P. A. Andrekson, V. Torres-Company, P.-H. Wang, Y. Xuan, D. E. Leaird, M. Qi, and A. M. Weiner, "Long-haul coherent transmission using a silicon nitride microresonator-based frequency comb as WDM source", *Conference on Lasers and Electro-Optics (CLEO)*, San Jose, USA, paper SM4F.2, 2016.

[O] M. Rezagholipour Dizaji, C. J. Krückel, **A. Fülöp**, P. A. Andrekson, V. Torres-Company, L. R. Chen, "Silicon-rich nitride waveguides for ultra-broadband nonlinear signal processing", *Optics Express*, vol. 25, no. 11, pp. 12100–12108, 2017.

[P] **A. Fülöp**, M. Mazur, A. Lorences-Riesgo, P.-H. Wang, Y. Xuan, D. E. Leaird, M. Qi, P. A. Andrekson, A. M. Weiner, V. Torres-Company, "PM-64QAM coherent optical communications using a dark-pulse microresonator frequency comb", *Conference on Lasers and Electro-Optics (CLEO)*, San Jose, USA, *Accepted as invited*, 2018.

[Q] Z. Ye, **A. Fülöp**, Ó. B. Helgason, P. A. Andrekson, V. Torres-Company, "Low loss silicon-rich silicon nitride for nonlinear optics", *Conference on Lasers and Electro-Optics (CLEO)*, San Jose, USA, *Accepted*, 2018.

[R] L. Lundberg, M. Mazur, **A. Fülöp**, V. Torres-Company, M. Karlsson, P. A. Andrekson, "Phase correlation between lines of electro-optical frequency combs", *Conference on Lasers and Electro-Optics (CLEO)*, San Jose, USA, *Accepted*, 2018.

[S] Ó. B. Helgason, **A. Fülöp**, J. Schröder, P. A. Andrekson, A. M. Weiner, V. Torres-Company "Superchannel engineering with microresonator combs", *Conference on Lasers and Electro-Optics (CLEO)*, San Jose, USA, *Accepted*, 2018.

[T] **A. Fülöp**, M. Mazur, A. Lorences-Riesgo, T. A. Eriksson, P.-H. Wang, Y. Xuan, D. E. Leaird, M. Qi, P. A. Andrekson, A. M. Weiner, V. Torres-Company, "Microresonator frequency combs for long-haul coherent communications", *International Conference on Laser Optics (ICLO)*, Saint Petersburg, Russia, *Invited*, 2018.

[U] V. Torres-Company, Z. Ye, **A. Fülöp**, C. J. Krückel, P. A. Andrekson, "High-confinement high-Q silicon-rich silicon nitride nonlinear microresonators", *OSA Advanced Photonics Congress*, Zürich, Switzerland, *Invited*, 2018.

Abbreviations

AWGN additive white Gaussian noise.
BER bit error ratio.
CMOS complimentary metal-oxide-semiconductor.
CW continuous-wave.
DSP digital signal processing.
EDFA erbium-doped fiber amplifier.
FEC forward error correction.
FSR free spectral range.
FWHM full width at half maximum.
FWM four-wave mixing.
LO local oscillator.
MI modulation instability.
MZM Mach-Zehnder modulator.
NLSE nonlinear Schrödinger equation.
OOK on-off keying.
OSNR optical signal-to-noise ratio.
QAM quadrature amplitude modulation.
RF radio frequency.
SNR signal-to-noise ratio.
WDM wavelength-division multiplexing.

Contents

Chapter 1

Introduction

The need to communicate and send messages between people has existed since the invention of the written word. For most of the history of humankind this has involved sending messages by carrier, either humans or carrier animals. While there are modern suggestions for carrying internet protocol packets using avian carriers [1], the vast majority of data traffic has been transmitted on lower-latency links for the past century. The first transatlantic telegraph cable was able to transmit a letter from queen Victoria to the president of the United States [2]. While this message allegedly took several hours to transmit, modern fiber-optic cables carry several terabits of data each second across more than 10 000 km [3]. The need for cheap and reliable transmission capacity, both over short and long distances, is however expected to keep increasing for the foreseeable future [4]. This need motivates the search for ever-higher performance and at the same time more power efficient methods of performing data transmission.

Fiber-optic technologies have been rapidly replacing electrical connections on increasingly short distances, from the transcontinental down to links of only a few meters in length. Key enabling technologies for this have been the semiconductor laser [5–8] and the low-loss optical fiber [9]. More recently the erbium-doped fiber amplifier (EDFA) [10] has enabled data transmission over long distances without the need for repeater stations. The EDFA has the ability to amplify optical signals across a bandwidth of several THz around wavelengths close to $\lambda = 1550\,\text{nm}$. This wavelength region also corresponds to the lowest loss region in the silica fiber's transparency window. To take advantage of the wide available transmission window, the concept of wavelength-division multiplexing (WDM) was introduced. WDM involves transmitting

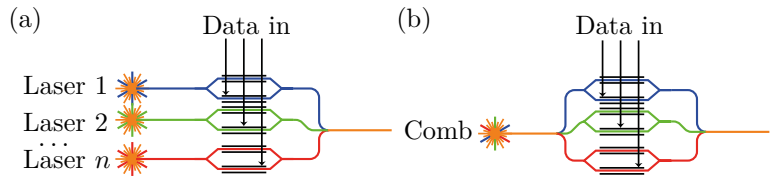

Figure 1.1. (a) Sketch showing a transmitter with several free-running lasers connected to modulators. (b) The same sketch with the lasers replaced by a single frequency comb source.

several data channels in parallel through the same physical fiber by using different wavelengths, all of which fit within the gain bandwidth of the EDFA.

In today's commercial WDM systems, an array of lasers, each operating at a slightly different wavelength, is used as light source. The laser light from each source is individually modulated with data after which they are recombined and transmitted down the link. A sketch of such a transmitter is shown in figure 1.1 (a). To help bring down the cost and power consumption of communications systems, various degrees of photonic integration have been developed over the past decades [11]. State-of-the-art demonstrations include complete multi-wavelength transmitters in indium phosphide [12], or complex multi-layer circuits in complimentary metal-oxide-semiconductor (CMOS)-compatible photonic circuits [13]. To further decrease the footprint of the transmitter and the control electronics, it is of interest to evaluate replacing the set of lasers with a single multi-wavelength light source. A chip-scale optical frequency comb, as shown in figure 1.1 (b), could provide this possibility.

Optical frequency combs in general are multi-wavelength light sources whose frequency lines are evenly spaced and phase-locked to each other. Looking at it from the time domain, this corresponds to a repetitive waveform with a repetition rate set by the frequency spacing of the comb lines. While mode-locked lasers qualitatively match this picture [14, 15], the first frequency combs where the central wavelength could be set freely were generated using electro-optic modulation of a continuous-wave (CW) laser tone [16]. These technologies have over the past decades enabled a large variety of communications demonstrations, including but not limited to Refs. [17–21]. More recently, it has been shown that combs with multi-GHz line spacing can be generated from a microresonator using a single pump laser [22, 23]. Microresonator combs made in a CMOS-compatible platform have the potential to allow co-integration of both optical and electrical components on a single chip [24]. This could revolutionize the availability of chip-scale multi-channel transceivers.

1.1 This thesis

The focus of this thesis is the usage of microresonator combs in the optical communications context. Previous work in this field indicate that microresonator combs hold great promise in enabling chip-scale multi-channel WDM data transceivers [25–27]. This thesis has focused on assessing their potential for long-haul communications and high-order modulation formats. An important distinction with respect to the quoted previous work is that we have focused on microresonators operating in the normal dispersion regime. This regime holds promises of high power conversion efficiency [28]. Ideally, a high power conversion efficiency be translated to a lowered pump power requirement or higher output comb line powers, ideally a combination of both!

Chapter 2 introduces the necessary concepts and performance metrics needed to understand and describe modern coherent optical communication systems. The chapter also gives a brief overview of the optical frequency comb technologies that have been employed and used in this field. In Chapter 3 the operational principle of microresonator frequency combs is described in detail. Following that, Chapter 4 will focus on and describe the stable frequency comb states that the microresonator systems can support. It will argue the pros and cons of each, with focus on the requirements for communication systems. Finally, in Chapter 5 we discuss what the near and mid-term future might hold. Following the appended papers, the Appendices will include schematics for code written in this project for the coherent receiver and for microresonator comb state simulations as well as a description of the stage setup used for the actual combs used in our lab.

Chapter 2

Optical frequency combs in coherent communications

2.1 Coherent communications systems

A generic point-to-point optical transmission system consists of a transmitter, the link itself and a receiver, see figure 2.1. Depending on the length of the link, it may consist of either a single span of fiber ($N_\mathrm{A} = 1$), or multiple ones requiring periodic amplification ($N_\mathrm{A} > 1$). For distances beyond a few kilometers, fiber-optic links today typically encode data on both the amplitude and phase of the optical field. By using both quadratures of the field, more data can be transmitted over the same bandwidth. To encode data on both quadratures (often called in-phase, I, and quadrature-phase, Q, in this context), a dual-drive Mach-Zehnder modulator (MZM) is typically used [29]. By programming the phases in the two arms carefully (denoted $\phi_1(t)$ and $\phi_2(t)$

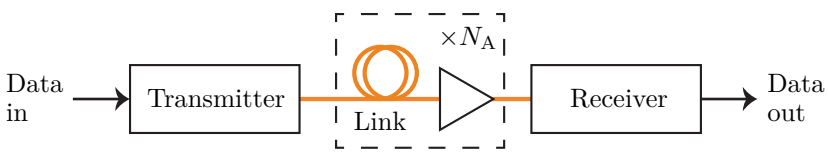

Figure 2.1. Sketch of a periodically amplified optical transmission link. After the target data is encoded by the transmitter, the link consists of N_A fiber spans, each followed by an amplifier to compensate for the fiber loss. At the end, a receiver decodes the transmitted data.

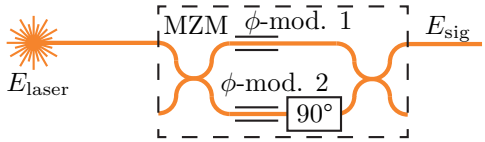

Figure 2.2. A sketch of a single-polarization transmitter containing a dual-drive MZM. In a dual-polarization setup, the outputs from two such modulators are combined with a polarization beam combiner.

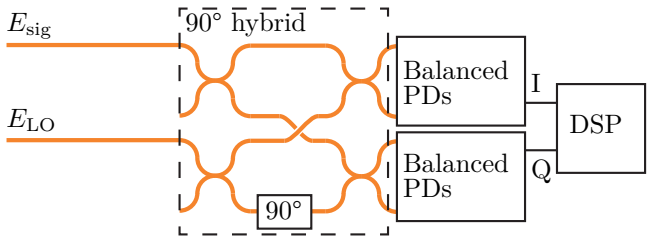

Figure 2.3. A sketch of a single-polarization coherent receiver showing the 90° hybrid with the 90° phase shifter and the balanced photodetectors. Extending this to a dual-polarization receiver requires putting a polarizing beam splitter and polarization rotator in front the signal input and duplicating the other components. The same LO can be used for both polarization channels at the cost of half its power.

in the equation below), both the amplitude and the phase of the final signal, E_{sig}, can be controlled independently:

$$E_{\text{sig}}(t) = \frac{E_{\text{laser}}}{2}\left(\exp(i\phi_1(t)) + i\exp(i\phi_2(t))\right). \tag{2.1}$$

On the receiver side, to decode the data on both the phase and the amplitude of the optical field, a coherent receiver is required. In a coherent receiver, the incoming optical signal is mixed together with a free-running local oscillator (LO) in an optical 90° hybrid. At the output of the hybrid, a pair of balanced photodetectors are placed from which one can extract the real as well as the imaginary part of the down-mixed field. A sketch demonstrating this setup is shown in figure 2.3. Constellation diagrams for some common modulation formats are shown in figure 2.4. By increasing the number of discrete levels in the I and Q planes, one can encode more bits in each symbol going from 2 bits/symbol in QPSK to 8 bits/symbol in 256QAM.

Once the down-mixed field is recorded, digital signal processing (DSP) can be used to recover the transmitted signal by removing the relative frequency offset of the LO. Later components of the DSP can then compensate for various

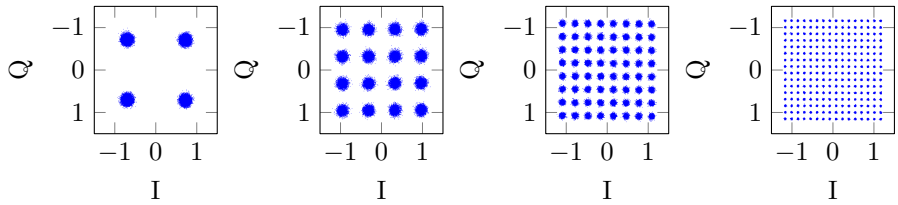

Figure 2.4. Constellation diagrams displaying all valid symbols for QPSK, 16QAM, 64QAM, and 256QAM. Note that for equal power normalization, the distances between the valid constellation points decrease as the order goes up resulting in higher sensitivity to added noise.

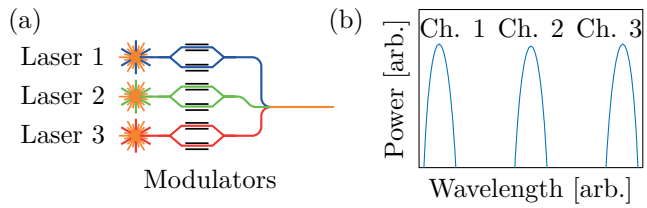

Figure 2.5. (a) Sketch of a three-channel WDM transmitter. The lasers operate at three different wavelengths and are modulated individually. (b) Sketch of the optical spectrum after the transmitter. The aggregate bandwidth of the transmitter increases proportionally with the channel count.

other signal impairments using a complex-valued equalizer. By knowing the used modulation format, the recovered signal can then be translated to a bit sequence. A diagram describing the DSP used in Paper D is included in Appendix A.

2.2 Wavelength-division multiplexing

Another important component in an optical communications system is the fiber link itself. The Shannon-Hartley theorem states that the maximum theoretical capacity in bits/s, C, of a Gaussian channel is proportional to the signal bandwidth, B [30]:

$$C = B \log_2 \left(1 + \frac{S}{N}\right), \tag{2.2}$$

where S is the total received electrical signal power and N is the total received electrical noise power. While the capacity provided by Equation 2.2 only

corresponds to a theoretical upper limit for a Gaussian channel, it provides guidance in the scaling laws of the physical quantities involved also for a fiber link. By encoding data onto multiple wavelengths, the total bandwidth, B, over which data is transmitted is increased, while the signal-to-noise ratio (SNR) S/N can remain constant leading to a linear increase in available capacity. The concept of WDM thus allows more data to be transmitted through the same physical fiber without requiring a corresponding increase in transmitter and receiver electrical bandwidth. Figure 2.5 provides a sketch of this concept.

At some point however, most real systems will reach a point where the effective bandwidth cannot be increased any further. This can be due to a lack of available matching components, such as amplifiers, or because there are other systems occupying neighbor frequencies. At that point the only way to increase the available capacity is to increase the SNR. In practice this also requires increasing the modulation format complexity. By encoding more bits of data into each transmitted symbol, the effective data rate will increase at the cost of higher sensitivity to the noise level. Section 2.3.1 will discuss in more detail how these requirements are connected.

2.3 Performance metrics and requirements

While the signal bandwidth provides one of the fundamental limits in communication systems, the SNR provides the other. In practice, measuring the electrical SNR of an optical channel is cumbersome as it requires receiving the signal and correcting for effects caused by the receiver. A simpler measurement, using an optical spectrum analyzer, can instead yield similar signal quality information through the optical signal-to-noise ratio (OSNR) metric:

$$\mathrm{OSNR} = \frac{P_{\mathrm{sig}}}{P_{\mathrm{n}}}, \tag{2.3}$$

where P_{sig} is the optical signal power in one channel and P_{n} is the noise power measured over a specified bandwidth $\Delta\nu_{\mathrm{OSA}}$ (typically 12.5 GHz or 0.1 nm). The OSNR metric can be translated to an electrical SNR under certain conditions [31, 32]. One has to assume that the data reception is performed using a coherent receiver and that the noise is dominated by additive white Gaussian noise (AWGN). This condition can typically be fulfilled by performing the OSNR measurement after the first amplifier in the link.

$$\mathrm{SNR} = \mathrm{OSNR}\frac{\Delta\nu_{\mathrm{OSA}}}{B}. \tag{2.4}$$

Here, $\Delta\nu_{\mathrm{OSA}}$ denotes the bandwidth over which the optical noise floor was measured while B denotes the channel bandwidth. A 25 GBd optical signal with 30 dB OSNR (measured using an optical spectrum analyzer at 0.1 nm resolution) will for example translate to a received electrical signal with 27 dB SNR. As OSNR lends itself to easy measurement, it is often used as a metric against which performance is compared. We will in the following sections talk about signal quality requirements in terms of minimum required OSNR, or signal impairments in terms of OSNR penalties.

The optical fiber is however also affected by intrinsic nonlinear effects. The optical power present in the fiber is directly (and deterministically) affecting the signal itself [33]. While numerically simulating such a nonlinear system is possible (see for example the propagation code described in Appendix B), predictions and estimations can be made without it. In a broadband WDM link (without optical dispersion compensation) where the data transmitted in each channel is uncorrelated, the nonlinear effects are noise-like [34]. They can therefore be modelled as such. This estimation allows calculating an effective OSNR after a link for each individual channel and is commonly known as the Gaussian noise model [35, 36]:

$$\mathrm{OSNR}_{\mathrm{eff}} \approx \frac{P_{\mathrm{sig}}}{P_{\mathrm{ASE,tot}} + \alpha P_{\mathrm{sig}}^3}, \tag{2.5}$$

where α is a constant depending on the link parameters including the fiber nonlinearity, the link length, and the number of channels. P_{sig} again corresponds to the power in a single channel, while $P_{\mathrm{ASE,tot}}$ is the accumulated white noise from the link amplifiers [31]:

$$P_{\mathrm{ASE,tot}} \approx N_{\mathrm{A}} 2 n_{\mathrm{sp}} h\nu \Delta\nu (G-1). \tag{2.6}$$

In the above equation, N_{A} denotes the number of amplifiers in the link while $2n_{\mathrm{sp}}$, $\Delta\nu$ and G denotes the amplifiers' noise figure, the bandwidth over which the noise is measured, and the gain of each amplifier. Since the effective noise at the receiver is now also increasing with transmitted signal power, there will in practice be an optimal launched signal power for any given link configuration.

2.3.1 Modulation-format dependent requirements

As a final step to be able to pose an OSNR requirement on a transmitter, one also has to select a target bit error ratio (BER) for the link. While error-free operation is typically wanted, a low error ratio, such as 10^{-15} (corresponding

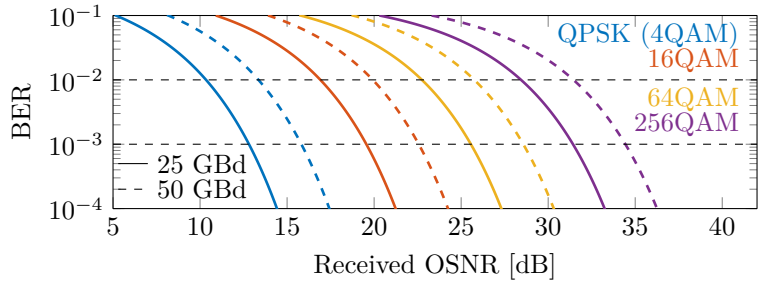

Figure 2.6. Bit error ratio as a function of received OSNR (noise floor measured with 12.5 GHz resolution) for various M-QAM modulation formats according to Equation 2.7. Note that doubling the modulation format order or doubling the symbol rate approximately corresponds to doubling the required OSNR.

to one bit error every three hours in a 100 Gb/s link), is often cited as a target for both research and commercial systems [37, 38]. For a system where the noise is dominated by AWGN, the BER can be related to the received OSNR according to [32]:

$$\mathrm{BER} \approx \frac{2}{\log_2(M)}\left(1-\frac{1}{\sqrt{M}}\right)\mathrm{erfc}\left(\sqrt{\frac{3}{2(M-1)}\frac{\Delta\nu_{\mathrm{OSA}}}{B}\mathrm{OSNR}}\right). \tag{2.7}$$

This equation is valid for M-ary quadrature amplitude modulation (QAM) formats under the assumption that Gray coding is used and that all symbol errors are between adjacent symbols. To illustrate the noise sensitivity of various common modulation formats Figure 2.6 shows the expected BER as a function of received OSNR.

In practice, applying a forward error correction (FEC) code to the link can be advantageous as it can allow significant relaxation of the received OSNR requirement. These algorithms allow increasing the link's BER target at the cost of data overhead [39]. A pre-FEC BER target between 10^{-3} and 10^{-2} is common among research papers (including appended papers A and D) where overheads of around 10% are accepted. From Equation 2.7 (or Figure 2.6), this can now be translated to a final modulation-format dependent minimum received OSNR requirement. To calculate a corresponding *transmitted* OSNR requirement, the expected link noise has to be calculated. Since the effective noise depends on the link length and the signal powers (as described in equation 2.5), to make an example calculation, we have to make some assumptions.

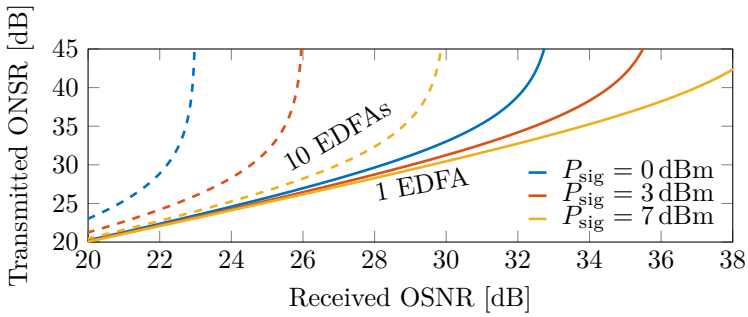

Figure 2.7. Required transmitted OSNR as a function of received OSNR for three different signal launch powers and two link lengths assuming fully linear propagation. The link represented by the fully drawn lines is assumed to contain a single EDFA with a noise figure of 5 dB operating at 20 dB gain while the dashed lines represent a link containing 10 such EDFAs. Note that by increasing the launch power we can make sure that the required transmitted OSNR stays similar to the received one.

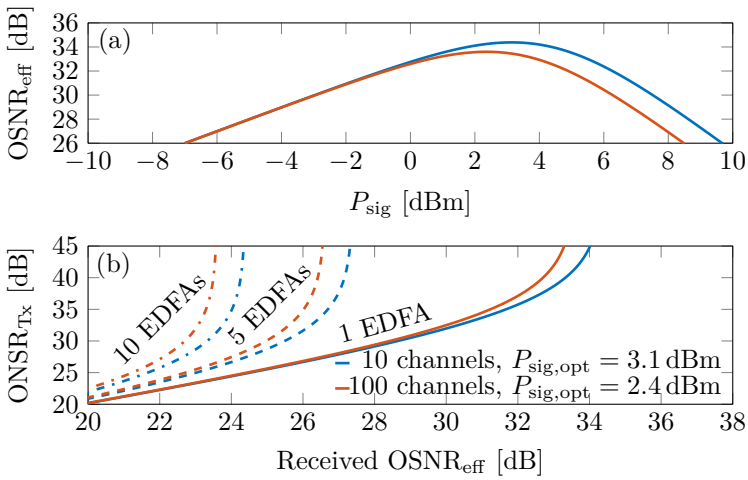

Figure 2.8. (a) Effective OSNR as a function of channel signal power after a single fiber span according to equation 2.5. The nonlinear link has 10 (blue) or 100 (red) channels containing signals with 50 GBd symbol rate. The EDFA is assumed to have a noise figure of 5 dB while operating at 20 dB gain to compensate for 100 km of single-mode fiber transmission. (b) Required transmitted OSNR as a function of received effective OSNR when the system is operating at the optimum launch power for 1, 5 and 10 fiber spans.

In a system without fiber nonlinearities, it is of interest to note that there will be no additional OSNR requirements on the transmitter. To compensate for the accumulating noise from the link amplifiers, one can simply increase the transmitted signal powers. Figure 2.7 shows the required OSNR at the transmitter side for a linear link for some cases of link length and launch power.

In a more realistic link, affected by fiber nonlinearities according to equation 2.5, there exists an optimum launch power above which the effective OSNR will decay, see Figure 2.8(a). Figure 2.8(b) displays the required transmitted OSNRs for an estimated received effective OSNR. To reach higher received effective OSNRs than figure 2.8 allows for (i.e. $> 35\,\mathrm{dB}$), one has to use shorter span lengths (i.e. $< 100\,\mathrm{km}$) or distributed amplification. It is important to note that the transmitted OSNR requirements apply *after* data modulation, any light sources in the transmitter will therefore likely need additional margin depending on penalties caused by the connected components.

2.3.2 Phase noise

While lasers are considered monochromatic light sources, they do have a non-zero linewidth and suffer from phase noise. Similarly to the OSNR, the phase noise requirements on the laser source will be modulation format dependent as high order formats encode information with higher density in the phase. The effect of phase noise on a coherent communication systems' BER has been under active investigation since the first coherent systems in the 80's [40]. The wish for a single-number quantity with which to describe laser phase noise has led to common usage of the 3 dB Lorentzian laser linewidth metric, $\Delta\nu_{\mathrm{L}}$. Often this is further normalized with respect to the symbol period: $\Delta\nu_{\mathrm{L}}T_{\mathrm{S}}$. Assuming a Lorentzian linewidth allows modelling the phase drift as a Wiener process where the drift between consecutive symbols is a zero-mean Gaussian random variable with variance $\sigma^2 = 2\pi\Delta\nu_{\mathrm{L}}T_{\mathrm{S}}$ [41, 42]. This permits the effect of a small amount of phase noise on the carrier to be translated to an OSNR penalty [42]. Putting it the other way, by accepting a certain OSNR penalty (e.g. 1 dB), one can estimate the required laser linewidth for a system. Figure 2.9 shows simulated trends for how the BER increases from an operating point of 10^{-3} as the laser linewidth is increased. Accepting a 1 dB penalty puts a clear limit on what amount of phase noise is accepted on the laser. In a real system however, one would probably pick the lasers in such a way that their linewidth does not dominate the BER (i.e. keeping the linewidths below where the curves start growing).

While a 3 dB linewidth provides a good metric with which to simulate lasers and to estimate DSP performance, it does not necessarily tell the whole picture.

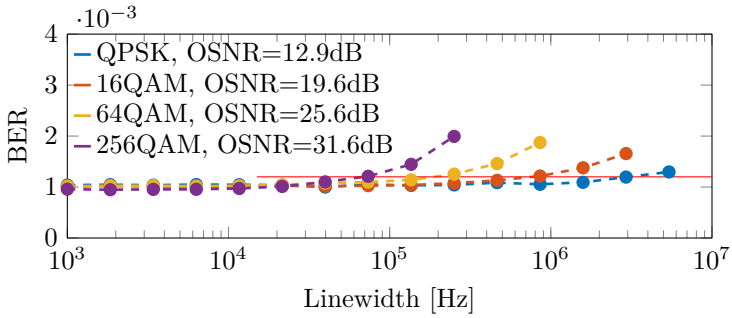

Figure 2.9. Simulated BER as a function of combined laser and local oscillator linewidth for various modulation formats at 25 GBd. The OSNR levels are chosen such that BER= 1×10^{-3} for a 0 kHz laser. The red line drawn at BER= 1.2×10^{-3} roughly corresponds to a 0.2 dB penalty according to figure 2.6.

The phase noise statistics of lasers have been known for some time not to be fully Lorentzian [43]. Typically it is the longer-term drift of the phase noise that doesn't conform [44]. At first guess, this will not significantly impact high symbol rate data transmission as the noise remains Lorentzian in the frequency region where the blind phase-tracking component of the DSP operates. This is however only true given that the non-Lorentzian noise component is weak and does not affect frequency regions of interest [45]. Of additional concern when it comes to optical frequency combs is the presence of any accumulating phase noise as one looks at comb lines far away from the center. Four-wave mixing tends to scale any uncorrelated phase noise in an unfavorable manner [46] while combs based on electro-optic modulation also show a small amount of scaling [47]. While scaling in microresonator comb sources is still an open research topic, in Paper B we performed measurements on one device to verify that any scaling stays within an order of magnitude. By selecting a sufficiently narrow linewidth pump laser, one can thereby ensure that all comb lines can be used for data communications. For guidance, table 2.1 contains received and transmitted OSNR and linewidth requirements for a set of common modulation formats and a single-span 100 km WDM link.

2.4 Optical frequency comb technologies

In the context of optical communications, optical frequency combs are currently treated as black-box multi-wavelength coherent light sources. While this is certainly a useful view, combs have wider use cases and properties that are

Modulation format	Symbol rate [GBd]	$OSNR_{Rx}$ [dB]	Linewidth [kHz]	No. channels	$OSNR_{Tx}$ [dB]
16QAM	25	19.6	860	200	20.0
	50	22.6	1 720	100	23.2
	100	25.6	3 440	50	26.5
64QAM	25	25.6	250	200	26.6
	50	28.6	500	100	30.6
	100	31.6	1 000	50	36.1
256QAM	25	31.4	75	200	36.3
	50	34.4	150	100	—
	100	37.4	300	50	—

Table 2.1. Table showing the OSNR and linewidth requirements for different modulation formats with a target BER of 10^{-3}. The $OSNR_{Rx}$ value is calculated using equation 2.7. The linewidth requirement is set to allow 0.2 dB OSNR penalty (BER= 1.2×10^{-3} according to figure 2.9). The required transmitted $OSNR_{Tx}$ includes the 0.2 dB penalty from the linewidth and is further assuming 100 km single-span transmission operating at optimum launch power with dense WDM, spanning 5 THz where the receiver has an EDFA with 5 dB noise figure (calculated the same way as in figure 2.8).

worth exploring.

As stated in the introduction, the first optical frequency comb sources were the electro-optic combs [16]. By modulating a laser externally using a phase modulator, one can set the resulting comb line spacing independently of the size of the laser cavity. Modern electro-optic frequency combs, using several cascaded phase modulators, can generate combs with more than 50 high-powered lines [48].

The bandwidth of a frequency comb can be significantly extended by amplification and successive broadening in a nonlinear medium. While nonlinear broadening in glass was observed already in the end of the 60's [49], so called supercontinuum generation spanning more than an octave was first reported using photonic crystal fibers and a mode-locked laser in 2000 [50]. By having access to an octave of bandwidth, the low-frequency part of the comb can be doubled and beat with the higher-frequency lines. This allows referencing and stabilizing the frequency comb with an external radio frequency (RF) reference [51]. This self-referencing technique has now also been demonstrated using broadening in highly nonlinear fiber with mode-locked lasers [52, 53], electro-optic combs [54, 55] and more recently with microresonator combs [56].

Stabilized optical frequency combs have been demonstrated to allow advances for a wide range of applications. Self-referenced combs permit measuring optical frequencies with the accuracy of RF references [57–59]. The technique of using combs as rulers [60, 61], against which calibrations can be made resulted in the physics Nobel prize of 2005. Applications include molecular spectroscopy [62–65], astronomy [66, 67] reaching all the way to attosecond scale measurements [68]. By using two combs in parallel, spectroscopic measurements of a sample's phase response also becomes practical [69–73]. Combs also allow for precise distance measurements on the nanometer scale using both time-of-flight [74] as well as interferometric [75, 76] techniques.

By detecting the pulse train from a frequency comb in a photodiode, combs can effectively be used as microwave synthesizers [77–80]. Furthermore, adjusting the frequency comb lines' relative amplitudes and phases allows for precise control of the pulse train's time domain shape. By combining a frequency comb with pulse shaping optics, one can thereby implement arbitrary microwave waveform generation [81, 82].

Not all applications require absolute frequency stability however. For applications such as optical communications, where a handful of relatively stable lines can be enough, comb sources producing fewer lines might make more sense. Integrated platforms provide a pathway to reduce the bulkiness of the comb sources, usually at the cost of line power or bandwidth. This can be interesting in applications where phase stability, power consumption or space availability provide critical constraints. Both electro-optic combs [83] and mode-locked lasers [84, 85] have been demonstrated in various integrated platforms. Integrated options however also include a new comb type: the microresonator combs [86]. In 2007, comb generation using whispering-gallery mode resonators consisting of silica-based toroidal microcavities was demonstrated [23]. Demonstrations in several other material platforms quickly followed including using CMOS-compatible planar silicon nitride rings [24, 87–89]. The working principle of these devices is the nonlinear Kerr effect [90]. Microresonator combs are usually pumped with a single or a few high-powered laser lines, which then through four-wave mixing cascade into a full comb. Assuming that the combs' line powers are high enough to meet the OSNR requirements discussed in the previous section, the combination of single-laser pumping and multi-GHz line spacing provide an attractive platform for multi-channel coherent communications experiments. The dynamics and function of these systems (including their soliton-like characteristics [89, 91]) is explored in more detail in the next chapter.

2.5 Combs as WDM light sources

By removing the need for multiple free-running lasers, mode-locked lasers and electro-optic frequency combs simplified early laboratory-based on-off keying (OOK) WDM scheme demonstrations [92]. A single electro-optic modulator fed with an RF oscillator doesn't yield a comb of significant bandwidth however. Demonstrations overcame this bandwidth limitation using nonlinear broadening [92]. By the year 2000, this allowed mode-locked laser-based sources to be used for the generation of over 1000 data channels [17]. A few years later, similarly broadened electro-optic combs were tested in a real-world link of about 100 km [18].

As discussed in Section 2.3, coherent modulation formats pose more strict requirements on the light source in terms of available OSNR and phase noise. Electro-optic combs have in the past few years been optimized to allow for increasingly high order formats, going from QPSK [93] to 16QAM [19, 94], 64QAM [20], and 128QAM [21]. While the spectral envelope of the broadened electro-optic combs can be kept flat [95], the phase noise of electro-optic combs scales quadratically as one moves away from the central wavelength [47]. This effect leads to varying OSNR penalties across the comb [19]. A way of minimizing this penalty is to instead modulate different formats on the carriers depending on their qualities (in terms of both OSNR and phase noise) [96]. Alternatively, one can elect to only use the highest quality lines in the comb, thereby pushing the modulation formats up to 256QAM [97].

The demonstrations quoted above all rely on a frequency comb providing a stable multi-wavelength light source replacing a rack of lasers. By only having to purchase a single low-linewidth laser, certain scenarios might this way allow for modulation formats with stricter linewidth requirements than what would otherwise be possible. To extract further gains from having a comb source will however require exploiting some of its unique coherence properties. By knowing in advance the exact frequency spacing of the data channels, it is possible to pre-compensate the signal in multiple channels for deterministic nonlinear effects caused by the fiber link [98, 99]. While the single-channel precompensation results in small gains also in laser-array based systems [100], comb-based few-channel scenarios have been shown to allow a doubling [101] or even tripling [102] of the transmission distance. Apart from enhancing nonlinearity-precompensation, stability of the channel spacing can be used to minimize the guard bands between adjacent channels, thus increasing the net spectral efficiency of broadband superchannels [21, 103, 104]. Additionally, comb lines are not only frequency-stable but also phase coherent. Recent demonstrations indicate that this phase coherence allows joint tracking of the

phase across several WDM channels yielding DSP simplifications [105].

The final topic of the frequency comb-based WDM source chapter is that of integration. A complete chip-scale transmitter where the comb generation and the data modulation can happen on the same chip has been a target which researchers have worked towards for some time. Current demonstrations typically contain a partially integrated comb source while the data transmitter remains set up using external discrete components. Initial integrated comb demonstrations using OOK modulation were done using quantum-dash mode-locked lasers [106] with microresonator comb demonstrations coming a few years later [107, 108]. Coherent modulation formats followed with quantum-dash mode-locked lasers enabling QPSK [109] up to 32QAM [110] modulation. Other integrated technologies include silicon-organic hybrid modulators [111] (note that electro-optic combs still require an external RF source in addition to the pump laser). Of main interest to this thesis are however the microresonator combs. Recent demonstrations include coherent communications over short distances [25, 26] in some cases with more than 100 comb lines [27]. Here, Paper D reaches all the way to PM-64QAM modulation with 20 lines. Paper A additionally proves that using QPSK and 16QAM long-haul links are also possible. These demonstrations prove that integrated comb sources, particularly microresonator combs, are now reaching a level where they can power modern coherent data communication links.

Chapter 3

Microresonator dynamics

The microresonator term is typically used to describe a millimeter-scale resonant cavity. In this chapter we will discuss planar microresonators, but the models are similar for Fabry-Perot cavities, microspheres, and other optical microcavity systems as well. Key features of microresonators are their small sizes (permitting resonance to be spaced by several tens of gigahertz) and their low roundtrip losses (corresponding to high quality factors). While optical microcavities can be used for a large array of topics [112], much of their functionality is centered around filtering and resonantly enhancing signals.

3.1 Microresonators in the linear regime

To describe the operating principle of microresonators, we first have to describe their linear, low-power operation. A microresonator is in the most basic view a two-component system: a directional coupler and a looped waveguide. Figure 3.1 shows a sketch where a second directional coupler (a drop port) has also been added. The complex electric fields at some notable positions has been indicated.

The coupling of the fields between the different paths can be described

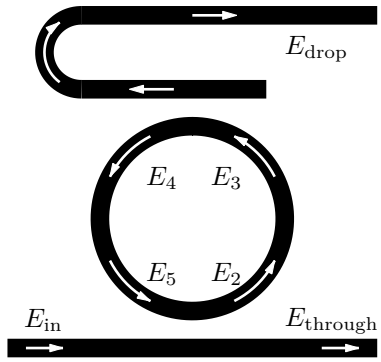

Figure 3.1. A sketch of a simple ring resonator system with both a through and a drop port.

using the following equations [113–116]:

$$\begin{bmatrix} E_{\text{through}} \\ E_2 \end{bmatrix} = \begin{bmatrix} t & \kappa \\ -\kappa^* & t^* \end{bmatrix} \begin{bmatrix} E_{\text{in}} \\ E_5 \end{bmatrix}, \tag{3.1}$$

$$\begin{bmatrix} E_{\text{drop}} \\ E_4 \end{bmatrix} = \begin{bmatrix} t_{\text{d}} & \kappa_{\text{d}} \\ -\kappa_{\text{d}}^* & t_{\text{d}}^* \end{bmatrix} \begin{bmatrix} 0 \\ E_3 \end{bmatrix}, \tag{3.2}$$

$$E_3 = \sqrt{a} \exp\left(i\beta \frac{L}{2}\right) E_2, \tag{3.3}$$

$$E_5 = \sqrt{a} \exp\left(i\beta \frac{L}{2}\right) E_4. \tag{3.4}$$

The two coupling regions are defined by the constants t, κ, t_{d}, and κ_{d}, such that $|t|^2 + |\kappa|^2 = 1$ and $|t_{\text{d}}|^2 + |\kappa_{\text{d}}|^2 = 1$. The ring waveguide loss is defined as $a = \exp\left(-\frac{\alpha}{2}L\right)$ where α is the power propagation loss per unit length and L is the physical length of the resonator. The propagation constant is denoted as β. The power out at the through and drop port can then directly be derived:

$$|E_{\text{through}}|^2 = |E_{\text{in}}|^2 \frac{|t|^2 + a^2|t_{\text{d}}|^2 - 2a|t||t_{\text{d}}| \cos(\beta L - \phi_t - \phi_{t,\text{d}})}{1 + a^2|t|^2|t_{\text{d}}|^2 - 2a|t||t_{\text{d}}| \cos(\beta L - \phi_t - \phi_{t,\text{d}})}, \tag{3.5}$$

$$|E_{\text{drop}}|^2 = |E_{\text{in}}|^2 \frac{a|\kappa|^2|\kappa_{\text{d}}|^2}{1 + a^2|t|^2|t_{\text{d}}|^2 - 2a|t||t_{\text{d}}| \cos(\beta L - \phi_t - \phi_{t,\text{d}})}. \tag{3.6}$$

The transmission coefficients have been expanded according to $t = |t| \exp(i\phi_t)$ and $t_{\text{d}} = |t_{\text{d}}| \exp(i\phi_{t,\text{d}})$. The case where there is no drop port can be trivially

extracted by setting $t_\mathrm{d} = 1$ and $\kappa_\mathrm{d} = 0$:

$$|E_\mathrm{through,nodrop}|^2 = |E_\mathrm{in}|^2 \frac{|t|^2 + a^2 - 2a|t|\cos(\beta L - \phi_\mathrm{t})}{1 + a^2|t|^2 - 2a|t|\cos(\beta L - \phi_\mathrm{t})}. \tag{3.7}$$

The above relations (particularly equation 3.5 and equation 3.7) will be useful for further derivations as they describe the system's spectral response.

3.1.1 Inter-waveguide coupling

The coupling parameter κ between two adjacent waveguides is naturally dependent on the interaction length and the mode overlap between the waveguides' transverse modes [117]:

$$\kappa_{12} \approx \omega\epsilon_0 \int (n_1^2 - n_\mathrm{cl}^2)\boldsymbol{e}_{\mathrm{t},1}^* \cdot \boldsymbol{e}_{\mathrm{t},2}\mathrm{d}x\mathrm{d}y, \tag{3.8}$$

where the tangential electric fields $\boldsymbol{e}_t$ are power normalized. The electric field values for the transverse modes of interest can be simulated using a standard mode solver. For well confined modes, the mode overlap will be low, leading to a weak coupling unless the interaction length is extended accordingly. The easiest way to increase the coupling interaction length is to make the bus waveguide follow the resonator over a part of a round-trip in a "pulley" coupling scheme [118] yielding an larger effective coupling parameter:

$$\kappa \approx \sin(\kappa_{12} L_\mathrm{pulley}). \tag{3.9}$$

In Paper D, this model permits motivating that power coupling parameters on the order of a few percent are achievable.

3.1.2 System characterization

To probe the system, we can make use of the fact that β depends on the probe laser frequency. This allows information about a and $|t|$ to be extracted from a sample by performing a scan with a tunable CW laser. Figure 3.2 shows an example of how such a scan should look like for a resonator without a drop port. Apart from the minimum power inside the resonance, it is possible to measure the resonance's FWHM. In the general case, the half maximum is defined as the point where the throughput power is exactly half-way between the minimum and the maximum. The measured $\Delta\omega_\mathrm{FWHM}$ can be translated to a $\Delta\beta_\mathrm{FWHM}$ according to:

$$\Delta\beta_\mathrm{FWHM} \approx \Delta\omega_\mathrm{FWHM} \frac{\partial\beta}{\partial\omega} \approx \Delta\omega_\mathrm{FWHM} \frac{n_\mathrm{g}}{c}. \tag{3.10}$$

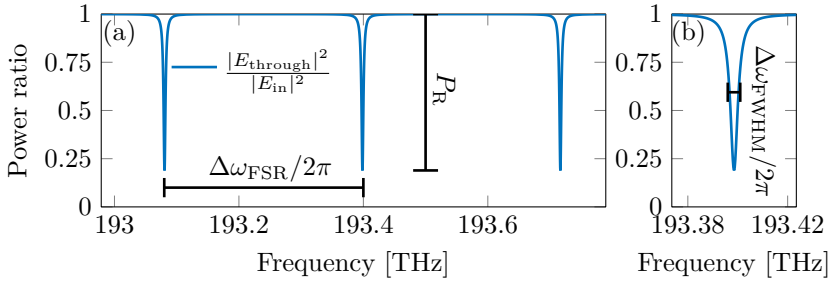

Figure 3.2. (a) Simulated scan for an undercoupled microresonator with the following parameters: $a^2 = 0.98$, $L = 2\pi 100\,\mu\text{m}$, $|t|^2 = 0.95$, $|t_\text{d}|^2 = 1$, $\phi_t = \phi_{t,\text{d}} = 0$, $\beta = n_\text{eff}\frac{2\pi}{\lambda}$, $n_\text{eff} = 1.5$. The extinction ratio, P_R, and the free spectral range (FSR) have been highlighted. (b) Zoomed-in view of one of the resonances. The resonance full width at half maximum (FWHM) has been highlighted.

Meanwhile, the expected $\Delta\beta_\text{FWHM}$ can be extracted from equation 3.5 [116]:

$$\Delta\beta_\text{FWHM} \approx 2\frac{1-a|t||t_\text{d}|}{L\sqrt{a|t||t_\text{d}|}}. \tag{3.11}$$

Setting equations 3.10 and 3.11 to equal yields the following relation between the FWHM and the losses:

$$\Delta\omega_\text{FWHM} \approx \frac{2c}{n_\text{g}L}\frac{1-a|t||t_\text{d}|}{\sqrt{a|t||t_\text{d}|}}. \tag{3.12}$$

To disentangle the contributions of the propagation loss, a, and the coupling loss, $|t|$, one can also look at the extinction ratio for the through port:

$$P_\text{R} = \frac{|E_{\text{through,max}}|^2}{|E_{\text{through,min}}|^2} = \frac{\left(1-a|t||t_\text{d}|\right)^2\left(|t|^2+a^2|t_\text{d}|^2\right)}{\left(a|t_\text{d}|-|t|\right)^2\left(1+a^2|t|^2|t_\text{d}|^2\right)} \approx \frac{\left(1-a|t||t_\text{d}|\right)^2}{\left(a|t_\text{d}|-|t|\right)^2}. \tag{3.13}$$

By measuring $\Delta\omega_\text{FWHM}$ and the extinction ratio, P_R, we can then, using equations 3.12 and 3.13, numerically extract the two parameters: $|t|$ and $a|t_\text{d}|$. In a system without a drop port we get the following set of equations:

$$\Delta\omega_\text{FWHM} \approx \frac{2c}{n_\text{g}L}\frac{1-a|t|}{\sqrt{a|t|}}, \tag{3.14}$$

$$P_\text{R} \approx \frac{\left(1-a|t|\right)^2}{\left(a-|t|\right)^2}. \tag{3.15}$$

To accurately convert between the resonance FWHM and the loss parameters, we need to know the group index, n_g, of the material. Fortunately, we can figure that out by finding the frequencies of two adjacent resonances and calculating the FSR: $\Delta\omega_{FSR} = |\omega_1 - \omega_2|$. We know that $|\beta(\omega_1)L - \beta(\omega_2)L| = 2\pi$. By assuming that the group index is identical for adjacent resonances (this assumption might not be valid for resonators with strong chromatic dispersion and large FSR!), we can extract:

$$n_g \approx \frac{2\pi c}{\Delta\omega_{FSR} L}. \tag{3.16}$$

It is now possible to numerically solve equation 3.14 and 3.15 for a and $|t|$. Note that the symmetry in the denominator of equation 3.15 will result in a pair of symmetrical solutions however. To distinguish an undercoupled resonator from an overcoupled one, further information is needed. This can be either through prior knowledge based on the system design or by measuring the phase response of the transmission scan.

3.1.3 Chromatic dispersion

As will become clear later in this chapter, the magnitude and the sign of the resonator waveguide's chromatic dispersion is also of great interest. One of the effects caused by the presence of chromatic dispersion is that the resonator's FSR becomes frequency dependent. We can use this knowledge to characterize it. By measuring the locations of three adjacent resonances, ω_{-1}, ω_0, and ω_1 (similar to figure 3.2), we can write the following equations:

$$\beta(\omega_0)L - \beta(\omega_{-1})L = 2\pi, \tag{3.17}$$

$$\beta(\omega_1)L - \beta(\omega_0)L = 2\pi. \tag{3.18}$$

After Taylor-expansion according to:

$$\beta(\omega_{\pm 1}) = \beta(\omega_0) + (\omega_{\pm 1} - \omega_0)\frac{\partial\beta}{\partial\omega}\bigg|_{\omega=\omega_0} + (\omega_{\pm 1} - \omega_0)^2 \frac{1}{2}\frac{\partial^2\beta}{\partial\omega^2}\bigg|_{\omega=\omega_0}, \tag{3.19}$$

we can directly extract the second order dispersion parameter:

$$\beta_2 = \frac{\partial^2\beta}{\partial\omega^2}\bigg|_{\omega=\omega_0} \approx \frac{2\pi}{L}\frac{\Delta\omega_{FSR}}{\overline{\omega_{FSR}}^3}, \tag{3.20}$$

where $\Delta\omega_{FSR}$ is the difference between the two adjacent FSRs and $\overline{\omega_{FSR}}$ is the average FSR. For a $\overline{\omega_{FSR}} \approx 2\pi \times 100\,\text{GHz}$ resonator, we need better than

$2\pi \times 1\,\mathrm{MHz}$ resolution in the $\Delta\omega_{\mathrm{FSR}}$ measurement to get β_2 with $100\,\mathrm{ps}^2/\mathrm{km}$ resolution however. To allow averaging (or extraction of higher order dispersion terms), one should measure a larger set of resonance locations symmetrically around ω_0. By performing a polynomial fit for all resonances to the following simple Taylor expansion, one can extract the dispersion parameters with increased precision:

$$(\omega_\mu - \omega_0)\beta_1 + (\omega_\mu - \omega_0)^2 \frac{\beta_2}{2} + (\omega_\mu - \omega_0)^3 \frac{\beta_3}{6} + \ldots = \mu \frac{2\pi}{L}. \tag{3.21}$$

In the above equation, μ is an integer describing the relative resonance number.

3.1.4 Quality factors

A common metric to characterize resonators in general is to calculate their Q-factors. This metric describes how many oscillations the electric field makes in the resonator before decaying (because of absorption or outcoupling). While this metric is in principle defined in the time domain, for high-Q resonators it relates to the FWHM of its resonances according to [116]:

$$Q \approx \frac{\omega}{\Delta\omega_{\mathrm{FWHM}}}. \tag{3.22}$$

When comparing different resonators to each other, it might be of interest to separate the loss effects caused by absorption and by outcoupling. One can in that case talk about *intrinsic* and *extrinsic* Q-factors. If a and $|t|$ have already been measured, equation 3.14 can estimate what the $\Delta\omega_{\mathrm{FWHM}}$ would be for a resonator either without propagation loss or without coupling to the environment. From that estimated resonance width, the following Q-factors can be calculated:

$$Q_{\mathrm{i}} \approx \frac{\omega n_{\mathrm{g}} L\sqrt{a}}{2c(1-a)} \approx \frac{\omega n_{\mathrm{g}}}{c\alpha}, \tag{3.23}$$

$$Q_{\mathrm{e}} \approx \frac{\omega n_{\mathrm{g}} L\sqrt{|t|}}{2c(1-|t|)}. \tag{3.24}$$

For systems with low losses (i.e. high Q-factors), it can be shown that $Q^{-1} \approx Q_{\mathrm{i}}^{-1} + Q_{\mathrm{e}}^{-1}$. Note that the Q-factors are proportional to the probing frequency, ω, as well as the resonator roundtrip length, L. Since both loss parameters (a and $|t|$) are defined per roundtrip, increasing both the frequency and the resonator length will proportionally increase the number of permitted electric field oscillations. When the losses are instead defined per unit length (as with α), the length-dependence goes away.

3.1.5 Optical confinement

The Q-factors are often mentioned in publications (including in the appended papers) as decreased losses correspond to longer (i.e. stronger) interactions. This can be understood by calculating the field intensity inside the resonator system. The relative intracavity power, or the on-resonance magnification, M, can be derived from equations 3.1 and 3.2 [114]:

$$M = \frac{|E_2|^2}{|E_{\text{in}}|^2} = \frac{1 - |t|^2}{\left(1 - a|t||t_{\text{d}}|\right)^2}. \tag{3.25}$$

For large Q-factors (i.e. when a and $|t|$ are close to 1), M is proportional to Q, meaning that measuring the Q-factor can give an estimation for the allowed intensity buildup inside the ring. Additionally it is worth noting that by decreasing the losses (increasing the Q-factor), the effective length along which interactions can occur is also increased. This will become important when considering nonlinear interactions later, as their strength will therefore be magnified quadratically with increasing Q.

3.1.6 Critical coupling

One potentially interesting special case is the situation of critical coupling. Critical coupling occurs when the coupling losses at the input are equal to the rest of the losses in the cavity:

$$|t| = a|t_d|. \tag{3.26}$$

In this situation, at resonance, equations 3.5 and 3.6 become:

$$|E_{\text{through}}|^2 = 0, \tag{3.27}$$

$$|E_{\text{drop}}|^2 = |E_{\text{in}}|^2 \frac{|t|}{|t_{\text{d}}|} \frac{1 - |t_{\text{d}}|^2}{1 - |t|^2}. \tag{3.28}$$

The ring absorbs the full power from the pump leaving nothing at the through port. If the resonator has a drop port, we can see from equation 3.26 that to maintain the critical coupling the propagation losses have to be decreased at the same rate as the coupling to the drop port is increased. In the special case of $|t_{\text{d}}| = |t|$, the absorption losses have to become zero! In this case the output power at the drop port, according to equation 3.28 will be equal to the input: $|E_{\text{drop}}|^2 \xrightarrow{t_{\text{d}} \to t} |E_{\text{in}}|^2$. The response of such a system is shown in Figure 3.3.

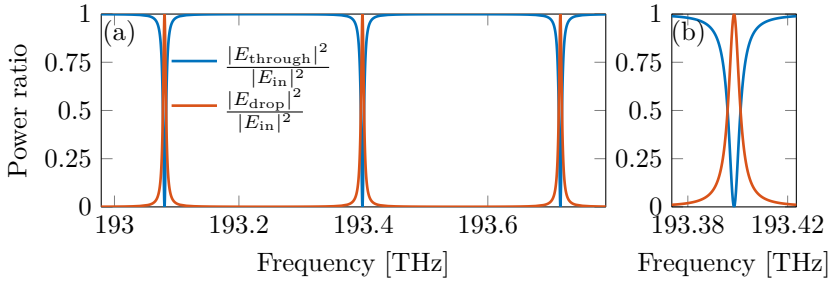

Figure 3.3. (a) Example scan for a critically coupled microresonator with the following parameters: $a = 1$, $L = 2\pi 100\,\mu\text{m}$, $|t|^2 = |t_\text{d}|^2 = 0.95$, $\phi_t = \phi_{t,\text{d}} = 0$, $\beta = n_\text{eff}\frac{2\pi}{\lambda}$, $n_\text{eff} = 1.5$. (b) Zoomed-in view of one of the coupling regions showing the symmetry between the two ports.

3.2 Nonlinear propagation

While equations 3.1–3.4 describe the filtering characteristics of resonators, to be able to model frequency comb states, the devices' nonlinear behavior has to be taken into account. Light-matter interaction in general is governed by Maxwell's equations. Their full analysis is beyond the scope of this thesis but can be found in reference [33]. They predict that for high optical intensities, such as the ones we will encounter inside the rings, the material will allow for nonlinear interactions between photons of different wavelengths. The part that concerns us the most is the interaction facilitated by the third-order susceptibility, $\chi^{(3)}$, causing the effective index of the mode in the material to be intensity-dependent [33]:

$$n(I) = n_\text{eff} + n_2 I(t). \tag{3.29}$$

To analyze waves propagating through a fiber or a waveguide, it is typically enough to model the field envelopes, A, rather than the electric field itself, where the amplitude is normalized such that $|A|^2 = I$. With this assumption, one can derive the nonlinear Schrödinger equation (NLSE) for the propagating waves [33]:

$$\frac{\partial A}{\partial z} = -\frac{\alpha}{2}A + i\sum_{k\geq 2}\frac{\beta_k}{k!}\left(i\frac{\partial}{\partial t}\right)^k A + i\gamma|A|^2 A. \tag{3.30}$$

Here, α denotes the fiber power losses per unit length while β_k denotes the k-th coefficient in the Taylor expansion of the frequency-dependent propagation

constant of the material. The nonlinear parameter, γ, is related to the intensity-dependent refractive index, n_2, and the effective mode area, A_{eff}:

$$\gamma = \frac{\omega_0 n_2}{c A_{\text{eff}}}. \tag{3.31}$$

The value of A_{eff} can be simulated both for fibers and waveguides (also for non-transverse electromagnetic modes [119]) allowing estimations of the γ parameter. For materials where tabulated data is scarce or inconsistent, this gives enough confidence in the order of magnitude to allow system simulations.

3.3 The Ikeda map

By modifying equations 3.1–3.4 to include the NLSE from equation 3.30, the nonlinear dynamics of the complete system can be explored. From here on, to simplify the analysis, we will focus on systems without a drop port, as shown in Figure 3.4. The transmission over one coupling region is further assumed not to change the phase: $\kappa = -\sqrt{\theta}$ and $t = \sqrt{1-\theta}$. Since we're working with the field envelope in the NLSE, the phase evolution over one roundtrip will not be present. A corresponding relative phase offset, ϕ is therefore included in the equation:

$$\begin{bmatrix} A_{\text{through}} \\ A_2 \end{bmatrix} = \begin{bmatrix} \sqrt{1-\theta} & -\sqrt{\theta} \\ \sqrt{\theta} & \sqrt{1-\theta} \end{bmatrix} \begin{bmatrix} A_{\text{in}} \\ A_3 \end{bmatrix}, \tag{3.32}$$

$$A_3 = \exp(-i\delta_0) \int_0^L \frac{\partial A(z,t)}{\partial z} \mathrm{d}z, \tag{3.33}$$

$$\text{where } A(0,t) = A_2.$$

The phase offset, δ_0, corresponds to the relative phase shift of the wave compared to the phase of a wave at a resonance wavelength: $\delta_0 = -\Delta\beta L \approx (\omega_{\text{mode}} - \omega_{\text{pump}}) \frac{L n_{\text{g}}}{c}$ and is applied at the end of each roundtrip.

This system model is sometimes called an Ikeda map after Ref. [120]. It allows simulations to be conducted using standard NLSE solvers (such as the split-step method described in Ref. [33]) by iterating the coupling region and the propagation element [121, 122]. As new pump light is coupled in at each roundtrip, it also allows correct noise handling [121]. The simulations included in Paper D were performed using this method. Appendix B contains a more detailed description of the algorithm.

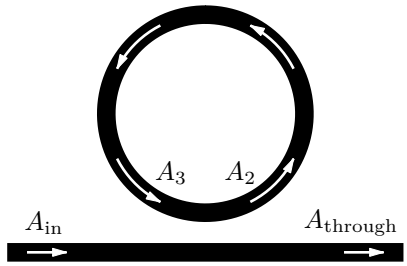

Figure 3.4. Sketch of a microresonator system with a single coupling region. The amplitude fields at the noted locations are used in the equations in the text.

3.4 The Lugiato-Lefever equation

While using the Ikeda map method to run system simulations works well, it is challenging to work with the model analytically. To get a single closed form expression that we can derive understanding from, we will have to make some additional assumptions and simplifications. We will assume that the field envelope barely changes over one roundtrip: $A(L,t) \approx A(0,t) + L\frac{\partial A}{\partial z}$. The equations governing the field inside the resonator cavity can then be rewritten as:

$$A_2 = \sqrt{\theta}A_{\text{in}} + \sqrt{1-\theta}A_3, \tag{3.34}$$

$$A_3 = \exp(-i\delta_0)\left(A_2 + L\frac{\partial A}{\partial z}\right). \tag{3.35}$$

Assuming that we have a weakly coupled resonator pumped close to a resonance, both θ and δ_0 are small. We can then Taylor expand them according to:

$$\sqrt{1-\theta} \approx 1 - \frac{\theta}{2}, \tag{3.36}$$

$$\exp(-i\delta_0) \approx 1 - i\delta_0. \tag{3.37}$$

Inserting this back into equations 3.34 and 3.35 and linearizing in terms of the variables θ, δ_0, and $\frac{\partial A}{\partial z}$ gives us an expression for the intracavity field after roundtrip m:

$$A_2^{(m)} \approx \sqrt{\theta}A_{\text{in}} + A_2^{(m-1)}\left(1 - \frac{\theta}{2} - i\delta_0\right) + L\frac{\partial A}{\partial z}. \tag{3.38}$$

We can now insert the NLSE from equation 3.30. Since we know that the change between consecutive roundtrips is small, we can write a differential equation describing the slow time-evolution of the wave at this point assuming a roundtrip time of t_r [123, 124]:

$$\begin{aligned}\frac{\partial A}{\partial \tau} &\approx \frac{A^{(m)} - A^{(m-1)}}{t_\mathrm{r}} \\ &= \frac{1}{t_\mathrm{r}}\left[\left(-\frac{L\alpha+\theta}{2} - i\delta_0 + iL\sum_{k\geq 2}\frac{\beta_k}{k!}\left(i\frac{\partial}{\partial t}\right)^k + i\gamma L|A|^2\right)A + \sqrt{\theta}A_\mathrm{in}\right].\end{aligned} \tag{3.39}$$

This equation is generally known as the Lugiato-Lefever equation or the driven-and-damped nonlinear Schrödinger equation. It has been used to describe ring cavities of fibers and other Kerr media and since the early 90's [125, 126]. It has more recently also been shown to be practical for modelling and simulating microresonator systems [124, 127]. As long as the pump detuning is not too large and the coupling strength is not too strong (i.e. while equations 3.36 and 3.37 are valid), it remains a powerful tool for analyzing the system dynamics. The Lugiato-Lefever model can be enhanced by including further physical effects including Raman scattering [128, 129], self-steepening [130], second order susceptibility [131–133] as well as thermal shifts [134, 135].

3.5 Bi-stability and comb initialization

Using the Lugiato-Lefever model from equation 3.39, it is then possible to analyze the behavior of microresonator systems. A perturbation analysis around a CW steady-state gives useful information about the system's dynamics when pumping with a single CW pump [121, 125, 126, 136–138]. The CW steady-state, A_s, can be found by setting all time derivatives in equation 3.39 to zero:

$$0 = \left(-\frac{L\alpha+\theta}{2} - i\delta_0 + i\gamma L|A_\mathrm{s}|^2\right)A_\mathrm{s} + \sqrt{\theta}A_\mathrm{in} \Rightarrow \tag{3.40}$$

$$\theta|A_\mathrm{in}|^2 = |A_\mathrm{s}|^2\left(\left(\frac{L\alpha+\theta}{2}\right)^2 + \delta_0^2\right) - |A_\mathrm{s}|^4 2\delta_0\gamma L + |A_\mathrm{s}|^6\gamma^2L^2. \tag{3.41}$$

Depending on the pumping region, equation 3.41 has between one and three solutions for $|A_\mathrm{s}|^2$. Figure 3.5 shows the steady-state solutions as the detuning,

δ_0, and the pump power, $P_{\text{pump}} = |A_{\text{in}}|^2$, are varied. Note that the curve depicting the intracavity power as a function of detuning in figure 3.5(a) turns into a Lorentzian when $\gamma = 0$. In that system, the FWHM matches the value for $\Delta\beta L$ extracted in the previous section (equation 3.11). It is furthermore worth noting that only the top and bottom CW solutions are stable (similarly corresponding to the top and bottom branch in figure 3.5(b)) [123].

While a more complete analysis of the system behavior is presented in Refs. [137, 138], it is of interest to take a quick look at what is required to de-stabilize a CW solution. Any modulation instability (MI)-like behavior is likely key to being able to generate a comb state from an empty cavity with only a CW pump laser. Choosing the following ansatz allows for finding MI gain regions [125, 136]:

$$A = A_{\text{s}} + A_{-1}(\tau)\exp(-i\Delta\omega t) + A_1(\tau)\exp(i\Delta\omega t). \tag{3.42}$$

Under the assumption that $|A_{-1,1}| \ll |A_{\text{s}}|$, the system experiences gain at frequencies offset from the pump, $\Delta\omega$, according to:

$$G(\Delta\omega) = \frac{1}{t_{\text{r}}}\left(-\frac{L\alpha+\theta}{2} + \sqrt{\gamma^2L^2|A_{\text{s}}|^4 - \left(2\gamma L|A_{\text{s}}|^2 - \delta_0 + L\sum_{k\geq 2,\text{even}}\frac{\beta_k}{k!}\Delta\omega^k\right)^2}\right). \tag{3.43}$$

Important to note is that for there to be net gain, the term under the square root has to remain positive and be large enough to compensate for both the propagation losses and the coupling losses. Figure 3.6 shows an example gain spectrum. For the gain to be maximized at a certain frequency offset, $\Delta\omega$, there will therefore be requirements on the physical parameters:

$$2\gamma L|A_{\text{s}}|^2 - \delta_0 + L\sum_{k\geq 2,\text{even}}\frac{\beta_k}{k!}\Delta\omega^k = 0. \tag{3.44}$$

This means that either negative even dispersion orders or a positive δ_0 is needed to achieve MI-based gain. Typically, the second order dispersion, β_2, is dominating this term, but examples have been shown where the presence β_4 makes a significant difference [139]. To avoid the global negative effective β_2 requirement one can design the waveguide so that the dispersion becomes anomalous only locally around the pump wavelength. In multi-mode waveguides the geometry can be designed so that higher order modes couple to the

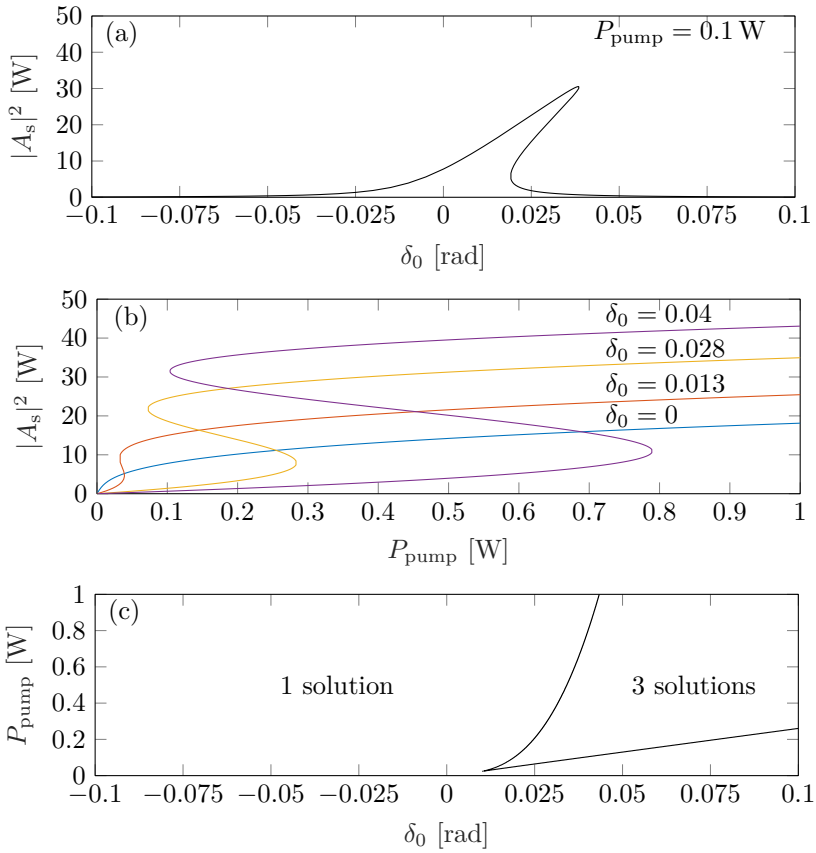

Figure 3.5. Bistability curves showing the intracavity power as a function of (a) the detuning, and (b) the pump power. (c) Contour plot showing the number of CW steady-state solutions for each combination. In all cases the rest of the parameters are fixed according to: $\alpha = 0.1\,\text{dB/cm}$, $L = 2\pi \times 100\,\mu\text{m}$, $\theta = 0.01$, and $\gamma = 2\,\text{W}^{-1}\text{m}^{-1}$, which are realistic for Si_3N_4-based microresonators.

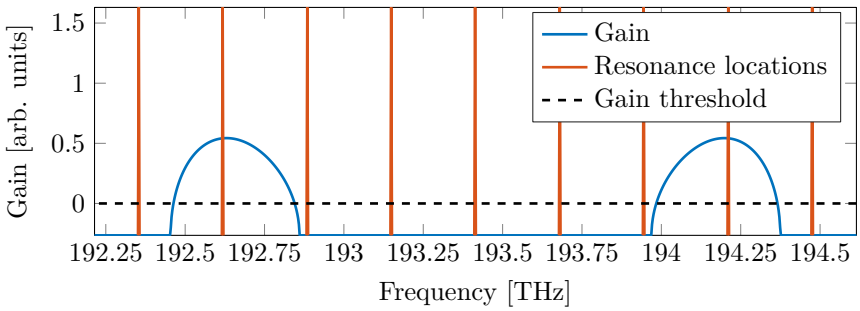

Figure 3.6. An example initial gain spectrum for a ring with the resonance locations plotted on top.

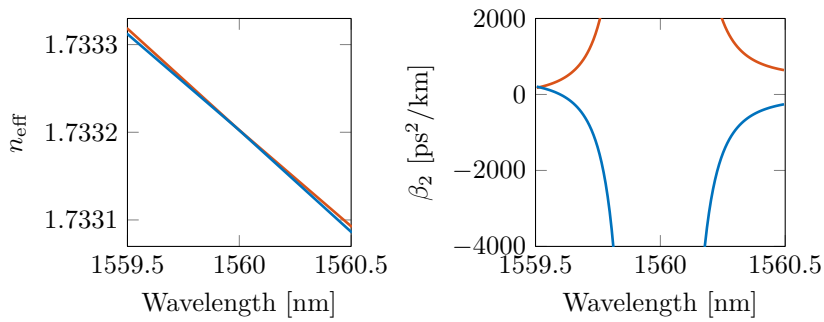

Figure 3.7. Simulated example where two modes interact. (Left) showing the effective index, n_{eff}, with the barely avoided crossing and (Right) showing the resulting perturbed dispersion, β_2 for the two modes.

pumped mode at some wavelength leading to a locally strong perturbation of the dispersion [91, 140–144]. Figure 3.7 shows how this would look like for two coupled modes. The resonators used in Papers A-D are enabled using such an interaction. In these circumstances the comb is initialized using the degenerate four-wave mixing (FWM) process that was described above, while the new lines are then grown using non-degenerate FWM (that has no requirements on the sign of the dispersion).

3.6 Thermal effects and detuning

The refractive index of most materials is temperature-dependent. Since microresonators are typically pumped with high-powered laser light, the temperature of chips under operation is expected to be higher than room temperature. When tuning a pump laser into a resonance, more and more power gets coupled into the ring, thus increasingly heating it up. This causes a red-shift of the resonance for most material platforms, including silicon nitride [145]. Since the resonances shift towards longer wavelengths regardless of the direction of the pump sweep, this leads to an asymmetric transmission scan that is different depending on the sweeping direction [146]. In practice, this also means that only a blue-detuned pump can be thermally stable. A small increase in the pump wavelength will cause the resonance location to shift away from the pump in the red-detuned case at which point the power level in the resonator decreases and causes the resonance to shift even further. Paper E as well as Ref. [146] show this in action.

While this seemingly makes any state requiring $\delta_0 > 0$ impractical to achieve, it is worth noting that the Kerr effect also shifts the resonance in the same direction [145]. As seen in figure 3.5(a), the upper bi-stable branch has $\delta_0 > 0$ even though it is blue-detuned from the resonance peak. The net pump detuning will therefore correspond to the sum of the Kerr phase shift and the unloaded resonance detuning:

$$\delta_{\text{net}} = \delta_0 - \phi_{\text{Kerr}} \tag{3.45}$$

$$= \delta_0 - \gamma P L. \tag{3.46}$$

As the intracavity power, P, close to resonance can reach several tens of Watts (in proportion to Q as described in Section 3.1.5), CW solutions can remain stable for small positive detunings. For solutions involving pulse forms beyond the CW state, a basic net detuning analysis can be made by looking at the phase shift accumulated by the CW pump during one roundtrip [28].

Chapter 4

Basic soliton dynamics in microresonators

In the previous chapter, we discussed the availability of several CW steady-state solutions to the Lugiato-Lefever equation. From these solutions, given that certain boundary conditions are met (described in equation 3.44), MI-like parametric gain can be achieved. While MI gives a hint at what comb initialization might look like, there is a richer dynamics available in nonlinear microresonators allowing several possible stable comb states. These include Turing patterns and circulating bright cavity solitons and dark pulses [147]. This chapter aims at discussing these stable comb states and their properties, particularly with respect to the metrics presented in Chapter 2.

4.1 Stable comb states

Perhaps the most intuitive comb states worth mentioning are those where the MI growth has cascaded into multiple comb lines and stabilized. These states go by the names of coherent MI combs or Turing patterns [147–150] after Alan Turing's work on pattern formation in nature [151]. Turing pattern-based comb states have been shown to be stable and robust towards external perturbations [26, 150]. Figure 4.1 shows an example case of a stable MI-based comb with a 37 FSR line spacing matching the locations predicted in the previous section by equation 3.44. Nevertheless, the limited line numbers (as seen in Paper A and Refs. [26, 152]) have constrained their use in coherent communications experiments.

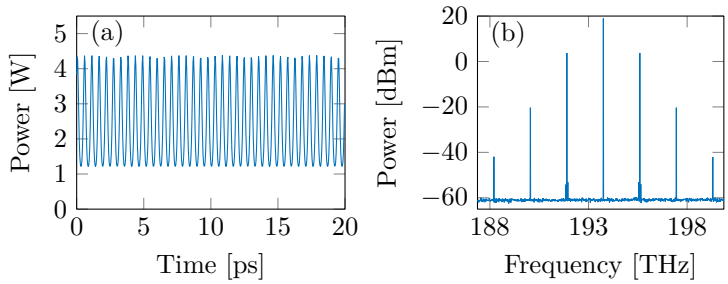

Figure 4.1. Simulated MI comb in a 50 GHz resonator. The plots show the 37 FSR-spaced comb's (a) intracavity time-domain picture and (b) outcoupled spectrum. The comb parameters are as follows: $\beta_2 = -200\,\mathrm{ps}^2/\mathrm{km}$, $\theta = 0.02$, $\alpha = 0.1\,\mathrm{dB/cm}$, $n_\mathrm{g} = 2$, $\gamma = 2\,\mathrm{W}^{-1}\mathrm{m}^{-1}$, $P_\mathrm{in} = 20\,\mathrm{dBm}$, $\delta_0 = -0.01\,\mathrm{rad}$.

4.2 Bright solitons

In the anomalous dispersion regime, Turing pattern-based combs can be turned into bright cavity soliton states [87, 89, 148, 153]. They can typically be generated by careful tuning of the CW pump into the resonance. When tuning in a straight-forward manner (i.e. using linear ramping of the pump power or wavelength), the comb state has to go through a chaotic region however. The final state will thereby greatly depend on the initial noise conditions [121, 148, 153, 154]. It has however been shown that by taking a more advanced route in terms of ramping the pump power and detuning, this chaotic regime can be avoided [155]. In practice, reaching a stable single-soliton state requires feedback from the experimental setup [89, 156, 157]. Recently, several groups have shown that using careful tuning methods, this can allow for deterministic single-soliton generation by tuning the laser wavelength [158, 159] or the chip temperature [160].

The final steady-state can be described as the sum of a low-power CW wave (corresponding to the lower branch of the CW steady-state solutions) and a soliton pulse. For a lossless resonator system, the soliton pulse can be derived analytically from the Lugiato-Lefever equation [89, 148, 161, 162]:

$$A_\mathrm{cs}(t) = \sqrt{\frac{2\delta_0}{\gamma L}}\,\mathrm{sech}\left(t\sqrt{\frac{2\delta_0}{|\beta_2|L}}\right). \tag{4.1}$$

The above equation corresponds to a soliton with the following total energy,

E_{cs}, and pulse duration (at FWHM), $\Delta t_{\mathrm{cs,3dB}}$:

$$E_{\mathrm{cs}} = \int_{-\infty}^{\infty} |A_{\mathrm{cs}}(t)|^2 \mathrm{d}t = \frac{2}{\gamma}\sqrt{\frac{2\delta_0|\beta_2|}{L}}, \tag{4.2}$$

$$\Delta t_{\mathrm{cs,3dB}} = \sqrt{\frac{2|\beta_2|L}{\delta_0}}\log(1+\sqrt{2}). \tag{4.3}$$

This detuning-dependence of the soliton energy allows stabilizing the comb state without direct measurement of the detuning parameter [159]. In the above equations, the detuning looks like a free parameter. It also seems like maximizing it is of interest to achieve narrower (i.e. higher bandwidth) and stronger (i.e. higher conversion efficiency) solitons. In a real system with losses from absorption and outcoupling however, boundary conditions exist for it. The upper limit permitting stable bright solitons has been shown to be [137, 148, 162]:

$$\delta_0 \leq \frac{\pi^2}{8}\frac{\gamma L\theta P_{\mathrm{in}}}{(\alpha L+\theta)^2/4}. \tag{4.4}$$

In the following equations and text, we will assume that we are always interested in the maximum allowed detuning. We can therefore replace the detuning parameter with the right-hand side of inequality 4.4. By comparing the outcoupled soliton energy, θE_{cs}, with the input pump power over one roundtrip time ($P_{\mathrm{in}}/\mathrm{FSR}$), the maximum possible conversion efficiency, η, can be calculated [128]:

$$\eta = \frac{2\pi\mathrm{FSR}}{\alpha L+\theta}\sqrt{\frac{|\beta_2|\theta^3}{\gamma P_{\mathrm{in}}}}. \tag{4.5}$$

To calculate the intra-cavity frequency spectrum of a soliton pulse, equation 4.1 has to be Fourier-transformed. When considering a pulse train of solitons, the envelope of the power spectral density also has to be multiplied by the repetition rate squared, yielding:

$$P_{\mathrm{env.}}(\omega) = 2\pi\frac{\pi|\beta_2|}{2\gamma}\mathrm{sech}^2\left(\omega\frac{\pi}{2}\sqrt{\frac{L|\beta_2|}{2\delta_0}}\right)\mathrm{FSR}^2. \tag{4.6}$$

By again setting the maximum allowed detuning according to inequality 4.4, we can calculate the pump-power dependent spectral envelope. Finally, to see

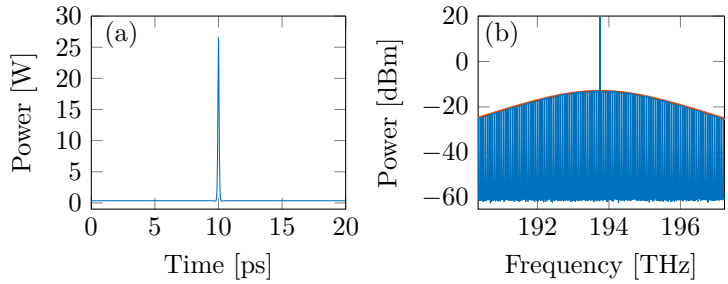

Figure 4.2. Simulated 50 GHz bright soliton comb showing the (a) intracavity time-domain picture and the (b) outcoupled spectrum. The red curve shows the expected theoretical envelope from equation 4.7. The comb parameters are as follows: $\beta_2 = -200\,\mathrm{ps}^2/\mathrm{km}$, $\theta = 0.02$, $\alpha = 0.1\,\mathrm{dB/cm}$, $n_\mathrm{g} = 2$, $\gamma = 2\,\mathrm{W}^{-1}\mathrm{m}^{-1}$, $P_\mathrm{in} = 20\,\mathrm{dBm}$, $\delta_0 = 0.077\,\mathrm{rad}$.

the outcoupled spectral powers, the coupling parameter, θ, has to be included:

$$P_{\mathrm{env.,out}}(\omega) = 2\pi\frac{\pi|\beta_2|}{2\gamma}\mathrm{sech}^2\left(\omega\frac{\alpha L+\theta}{2}\sqrt{\frac{|\beta_2|}{\gamma\theta P_\mathrm{in}}}\right)\mathrm{FSR}^2\theta. \tag{4.7}$$

As shown in figure 4.2(b), this equation provides a good fit to simulated comb states. From this, one can further calculate the soliton's 3 dB bandwidth in the frequency domain as well as the number of lines that fall within that bandwidth [128]:

$$\Delta f_{3\,\mathrm{dB}} = \frac{2\log(1+\sqrt{2})}{\pi(\alpha L+\theta)}\sqrt{\frac{\gamma\theta P_\mathrm{in}}{|\beta_2|}}, \tag{4.8}$$

$$N_{3\,\mathrm{dB}} \approx \frac{\Delta f_{3\,\mathrm{dB}}}{\mathrm{FSR}}. \tag{4.9}$$

From a comb use case perspective a few trends and trade-offs are worth highlighting [128, 148, 163]:

- An increased pump power increases the comb bandwidth (equations 4.7 and 4.8) while decreasing the power conversion efficiency (equation 4.5).
- Doubling the comb FSR quadruples the comb lines' powers (equations 4.6 and 4.7).
- The power conversion efficiency and number of generated comb lines are inversely related according to $\eta N_{3\mathrm{dB}} = 4\log(1+\sqrt{2})\theta^2/(\alpha L+\theta)^2$ (equations 4.5 and 4.9).

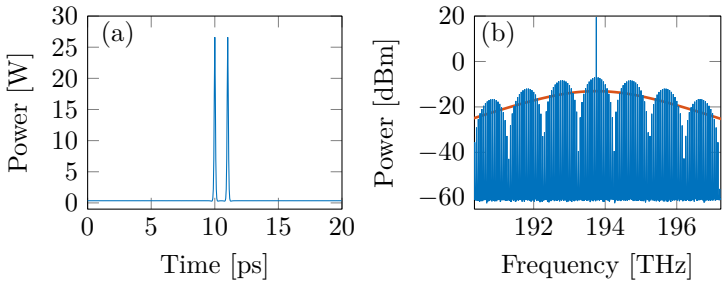

Figure 4.3. Simulated 50 GHz bright soliton comb containing two circulating pulses showing the (a) intracavity time-domain picture and the (b) outcoupled spectrum. The red curve shows the expected theoretical envelope from equation 4.7. The comb parameters are as follows: $\beta_2 = -200\,\mathrm{ps}^2/\mathrm{km}$, $\theta = 0.02$, $\alpha = 0.1\,\mathrm{dB/cm}$, $n_\mathrm{g} = 2$, $\gamma = 2\,\mathrm{W}^{-1}\mathrm{m}^{-1}$, $P_\mathrm{in} = 20\,\mathrm{dBm}$, $\delta_0 = 0.077\,\mathrm{rad}$.

In other words, there exists a fundamental trade-off between the number of lines, the pump power, and the outcoupled line powers. When it comes to applications, these bright soliton states have been shown to be capable of producing a large number of comb lines spanning wide bandwidths. This has enabled impressive data communications demonstrations spanning both optical C and L-bands providing aggregate data rates of several tens of terabits/s [27]. Self-referencing is enabled by combs spanning close to, or even surpassing an octave [135, 164]. This has enabled the prospect of an integrated optical-frequency synthesizer [165]. Other recent developments include dual-soliton systems enabling chip-based dual-comb spectroscopy [73] and fast sub-micrometer distance measurements [166, 167]. In the quoted demonstrations (and others), bright soliton combs have proven a level of maturity and stability allowing research to be conducted with them as black-box coherent multi-wavelength light sources.

As a note of curiosity: The single-soliton case is not the only stable bright soliton state available. After moving through the chaotic region during the initialization process, the system can converge to a state containing multiple circulating bright solitons [158, 159, 168]. Such a state is shown in figure 4.3. In this situation, the power conversion efficiency increases linearly with the number of solitons in the cavity! The resulting spectral envelope contains "holes" however prohibiting applications that require all lines to have high powers. These multi-soliton states have been proposed to be useful as optical buffers [169], however they constitute a complete research topic in themselves [170].

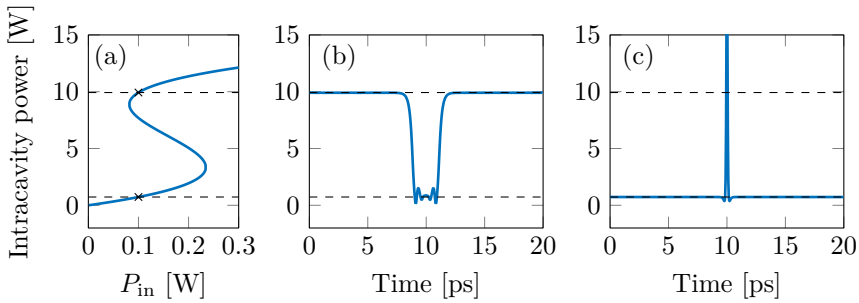

Figure 4.4. (a) Bistability curve showing the available CW solutions for a 50 GHz FSR microresonator system with parameters: $\theta = 0.02$, $\alpha = 0.1\,\text{dB/cm}$, $n_g = 2$, $\gamma = 2\,\text{W}^{-1}\text{m}^{-1}$, $\delta_0 = 0.0552\,\text{rad}$. The dashed lines mark the values for the upper and lower state solution with a 20 dBm pump. (b) Intracavity waveform for for a dark pulse solution (with $P_{\text{in}} = 20\,\text{dBm}$ and $\beta_2 = 200\,\text{ps}^2/\text{km}$). (c) Intracavity waveform for a bright cavity soliton solution (with $P_{\text{in}} = 20\,\text{dBm}$ and $\beta_2 = -200\,\text{ps}^2/\text{km}$).

4.3 Dark pulses

Recently it has been shown that a wide-bandwidth comb state can also be generated in the normal dispersion regime [91, 171]. One interesting aspect of these states is that the power conversion efficiency can reach $\eta > 30\%$ even with more than ~ 40 lines present [28, 172]. This is in contrast to similar bright soliton systems where η is typically limited to the order of a few percent. Whereas the bright solitons correspond to circulating bright pulses inside the resonator cavity, the broad-band normal-dispersion states can contain circulating dark pulses. While these states are in some ways analogous to the dark soliton solution in fibers, they have to comply with the periodic boundary condition imposed by the resonator. This prohibits the π phase change of the classical dark fiber solitons. Microresonator dark pulses have however successfully been described and simulated in the form of "platicons" [173, 174], or switching waves [175–179]. In contrast to the intracavity field for the bright cavity solitons that consists of the low-powered CW state and a pulse, the switching wave description approximates the dark pulses to switch between the low-powered CW state and the high-powered CW state. This difference is shown in figure 4.4. The features yielding a comb in the spectral domain can therefore be attributed to the transition between the two CW states. Similarly to the bright soliton combs, it is possible to stabilize a dark pulse in several steady states corresponding to a different order circulating dark pulse. Figures 4.5 and 4.6 show two such example cases with the bright

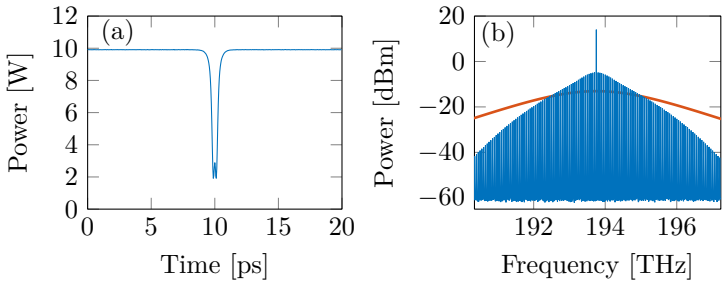

Figure 4.5. Simulated 50 GHz dark pulse comb showing the (a) intracavity time-domain picture and the (b) outcoupled spectrum. The red curve shows the expected theoretical envelope for bright solitons from equation 4.7. The comb parameters are as follows: $\beta_2 = 200\,\mathrm{ps}^2/\mathrm{km}$, $\theta = 0.02$, $\alpha = 0.1\,\mathrm{dB/cm}$, $n_\mathrm{g} = 2$, $\gamma = 2\,\mathrm{W}^{-1}\mathrm{m}^{-1}$, $P_\mathrm{in} = 20\,\mathrm{dBm}$, $\delta_0 = 0.0552\,\mathrm{rad}$.

soliton envelope overlaid. An important difference with regards to bright cavity solitons is that in the dark pulse state, the lobes resulting from entering a higher-order state do not result in weaker components in the spectrum. On the contrary, they help with broadening (and flattening!) the output comb spectrum.

An analytical analysis comparable to the bright solitons cannot be performed without a closed-form expression. Numerical analysis however (as will be described in Paper S) shows that the trends are very similar. In the same manner, increasing the comb bandwidth results in weaker comb lines overall. The design of a comb source will therefore be very much application-dependent. For communications, only comb lines within a set bandwidth (such as the C-band) are typically of interest. In Paper D, 20 comb lines within the C-band are generated using a dark pulse comb source pumped with less than 0.5 W off-chip power. Owing to the high ($> 20\%$) power conversion efficiency of the device, these lines allow data to be encoded using modern high-order coherent modulation formats.

As discussed in the previous chapter, the Lugiato-Lefever model predicts that for CW pumps (avoiding significant red detuning), a resonator needs anomalous dispersion to initialize a FWM process. Dark pulse combs however operate in the normal dispersion regime. To simulate dark pulse comb states, we therefore typically initialize the system with a square wave according to the levels of the bistability curve (as seen in figure 4.4 (a)) [91]. In this manner, the system converges to a dark pulse state without any ramping of the pump parameters. In a real-world system however, we do not have

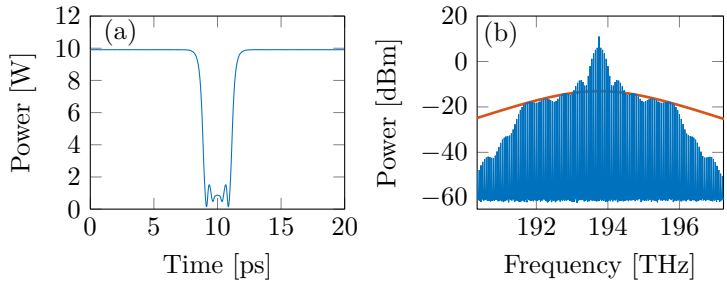

Figure 4.6. Simulated 50 GHz dark pulse comb containing a higher-order dark pulse showing the (a) intracavity time-domain picture and the (b) outcoupled spectrum. The red curve shows the expected theoretical envelope for bright solitons from equation 4.7. The comb parameters are as follows: $\beta_2 = 200\,\mathrm{ps}^2/\mathrm{km}$, $\theta = 0.02$, $\alpha = 0.1\,\mathrm{dB/cm}$, $n_\mathrm{g} = 2$, $\gamma = 2\,\mathrm{W}^{-1}\mathrm{m}^{-1}$, $P_\mathrm{in} = 20\,\mathrm{dBm}$, $\delta_0 = 0.0552\,\mathrm{rad}$.

the luxury of picking the starting conditions. Most demonstrated systems (including Refs. [91, 141] and the combs used in Papers A-D) are therefore enabled by multi-mode dynamics described in the previous chapter. As these systems are not tunable after fabrication, the comb's central wavelength is defined by the location of the modal coupling. By adding a second resonator to the system, it is possible to remove the multi-mode requirement for the comb generation [142, 180]. By thermally tuning the two resonators, their respective modes can couple in a tunable manner allowing post-fabrication control over the resulting comb's central wavelength. This has the potential to simplify and expand the possible scenarios where dark pulse combs can be useful.

Chapter 5

Future outlook

The results presented in this thesis provide a starting point for employing dark-pulse combs in coherent transmission applications. There are several paths along which one can continue however. Here, I will highlight two areas of personal interest:

- **Exploit comb coherence in transmission experiments.**

  As demonstrated in several publications including Refs. [25–27] and Papers A and D, microresonator combs are already today used in laboratory-based coherent communications experiments. These experiments however rely on the combs merely being a replacement for a set of lasers. While there are power efficiency gains to be had by using integrated comb sources (see for example the calculations in the supplementary material of Ref. [27]), they have the potential to yield further advantages. Experimentally proving that microresonator combs can allow for joint processing of several data channels (in terms of phase tracking, as with electro-optic combs in Ref. [105] or multichannel digital back-propagation as in Ref. [98]) as well as allowing dense channel spacing (as with electro-optic combs in Ref. [104]) would further increase their attractiveness. Enabling joint processing experiments will require using identical combs in the transmitter and receiver (as has been proven possible in Ref. [27]) together with a clever multi-channel transmitter and receiver setup. To enable demonstrations with ultra-dense channel spacing, microresonator combs are needed with line spacings on the order of 50 GHz. While manufacturing dense combs is challenging, recent demonstrations have included both bright solitons [181] and dark pulses [172].

- **Explore and optimize the operation of dark pulse combs.**

  One of the differences between the bright soliton and dark pulse comb states is their pump laser detuning. Whereas bright soliton states have been estimated and measured to operate in a net red-detuned manner [158, 182], dark pulse states are expected to stay on the blue side [28]. While the implications of this are not entirely clear, it is nevertheless a parameter that should be measured and verified experimentally.

  In Paper B we observed a small, yet noticeable, relative phase noise increase on microresonator comb lines located far away from the pump. This intriguing trend has at present no explanation and requires further analysis on combs of various types as it will likely have an effect on the performance of joint phase tracking algorithms.

  Finally, the optimized dark pulse comb states found in simulations (as discussed in the supplementary materials to Paper D and in what will be presented in Paper S) will require experimental verification. Key trends, including relationships between conversion efficiencies, comb line numbers and pump power requirements will have to be tested. Having access to these relations will be critical in designing optimal comb sources for optical communication systems of any bandwidth.

Chapter 6

Summary of papers

Paper A

"Long-haul coherent communications using microresonator frequency combs", *Optics Express*, vol. 25, no. 22, pp. 26678–26688, 2017.

In this paper we present the results from two coherent long-haul transmission experiments. We transmitted PM-QPSK-modulated data over more than 6000 km and PM-16QAM-modulated data over more than 700 km using a recirculating fiber loop. The light source consisted of seven (resp. six) lines generated using a low-noise microresonator-based frequency comb manufactured at Purdue University, USA. This is the first demonstration of long-haul data transmission using microresonator-based combs as light sources showing that the technology fits the requirements of long-haul data transmission. To describe the initialization mechanisms for the used combs, the paper also includes characterization of the mode coupling present in the resonator used for the second transmission experiment.

My contribution: I performed the transmission measurements with support from the co-authors, implemented the DSP code, characterized the mode coupling in the system, wrote the paper with support from the co-authors, and presented part of the results at CLEO in San Jose, USA in 2016.

Paper B

"Frequency noise of a normal dispersion microresonator-based frequency comb", *Optical Fiber Communications conference (OFC)*, Los Angeles, USA, paper W2A.6, 2017.

In this work, we perform initial characterizations of the frequency noise present in a normal dispersion microresonator comb. The microresonator was the same comb as the one used in the 16QAM transmission experiment in Paper A. We conclude that, while mostly depending on the pump laser, there are scaling effects present. While the scaling is small enough not to be noticed in the 16QAM experiment in Paper A, it is measurable.

My contribution: I performed the device characterization and data processing. I also wrote the paper with support from the co-authors and presented the work at OFC in Los Angeles, USA in 2017.

Paper C

"Active feedback stabilization of normal-dispersion microresonator combs", *European conference on Lasers and Electro-optics (CLEO Europe)*, Munich, Germany, paper CD-P-45, 2017.

In this work we set up a basic stabilization scheme for a dark-pulse microresonator comb. The microresonator was supplied by our collaborators at Purdue University, USA. By continuously measuring the outcoupled power and automatically adjusting the pump frequency when it was drifting, we could keep the total power in the comb stable over several hours.

My contribution: I performed the measurements and wrote the paper with support from the co-authors. I presented the work at CLEO Europe in Munich, Germany in 2017.

Paper D

"High-order coherent communications using mode-locked dark pulse Kerr combs from microresonators", *Under review.*

In this paper we present the results from a 20-channel coherent transmission experiment. We modulated data using PM-64QAM onto the lines of a dark-pulse microresonator comb fabricated at Purdue University. The results constitute the highest-order modulation formats encoded onto any integrated comb source to date. We furthermore kept the pump laser power at a level compatible with state-of-the-art integrated lasers. Together with included simulations using a more optimized comb, we claim that dark-pulse microresonator combs can at the same time be compatible with integrated power levels and high bit rate communications.

My contribution: I performed the transmission measurements together with the co-authors, implemented the DSP code, characterized the dark pulse state and the comb line spacing stability, and wrote the paper with support from the co-authors.

Paper E

"Triply resonant coherent four-wave mixing in silicon nitride microresonators", *Optics Letters*, vol. 40, no. 17, pp. 4006–4009, 2015.

Here we measured the changes in four-wave mixing efficiency inside a triply-pumped normal dispersion microresonator while varying the relative phases of the pump waves. The three waves were generated using a tunable laser and electro-optic modulator and were set to wavelengths matching three adjacent resonances in the microresonator. The microresonator was manufactured in a multi-project wafer run by LioniX in the Netherlands. Additionally a simplified analytical model was developed that qualitatively matches the measurements while more complete numerical simulations were performed that also match quantitatively. Simulations using similar pump parameters but with an anomalous dispersion resonator were also performed. The results of experiments, simulations and analytical model all indicate that controlling the relative phases in the pump waves is of critical importance when maximizing the four-wave mixing efficiency.

My contribution: I performed the measurements, calculated the model with support from the co-authors, implemented the simulations, and wrote the paper with support from the co-authors. I also presented the work at CLEO Europe in Munich, Germany in 2015.

References

[1] Internet Engineering Task Force. (1990). A standard for the transmission of IP datagrams on avian carriers, [Online]. Available: https://tools.ietf.org/pdf/rfc1149.pdf (visited on 01/29/2018).

[2] J. A. Spencer, "The Queen's message", in *History of the United States: from the earliest period to the administration of President Johnson: Vol. 3*, 1866, p. 542.

[3] NEC. (2014). A global consortium to build new trans-pacific cable system "FASTER", [Online]. Available: http://www.nec.com/en/press/201408/global_20140811_01.html (visited on 02/22/2018).

[4] Cisco. (2017). The zettabyte era: Trends and analysis, [Online]. Available: https://www.cisco.com/c/en/us/solutions/collateral/service-provider/visual-networking-index-vni/vni-hyperconnectivity-wp.pdf (visited on 02/22/2018).

[5] R. N. Hall, G. E. Fenner, J. D. Kingsley, T. J. Soltys, and R. O. Carlson, "Coherent light emission from GaAs junctions", *Physical Review Letters*, vol. 9, no. 9, pp. 366–368, 1962. DOI: 10.1103/PhysRevLett.9.366.

[6] M. I. Nathan, W. P. Dumke, G. Burns, F. H. Dill, and G. Lasher, "Stimulated emission of radiation from GaAs p-n junctions", *Applied Physics Letters*, vol. 1, no. 3, pp. 62–64, 1962. DOI: 10.1063/1.1777371.

[7] N. Holonyak and S. F. Bevacqua, "Coherent (visible) light emission from $Ga(As_{1-x}P_x)$ junctions", *Applied Physics Letters*, vol. 1, no. 4, pp. 82–83, 1962. DOI: 10.1063/1.1753706.

[8] T. M. Quist, R. H. Rediker, R. J. Keyes, W. E. Krag, B. Lax, A. L. McWhorter, and H. J. Zeigler, "Semiconductor maser of GaAs", *Applied Physics Letters*, vol. 1, no. 4, pp. 91–92, 1962. DOI: 10.1063/1.1753710.

[9] K. Kao and G. Hockham, "Dielectric-fibre surface waveguides for optical frequencies", *Proceedings of the Institution of Electrical Engineers*, vol. 113, no. 7, pp. 1151–1158, 1966. DOI: 10.1049/piee.1966.0189.

[10] R. Mears, L. Reekie, I. Jauncey, and D. Payne, "Low-noise erbium-doped fibre amplifier operating at 1.54µm", *Electronics Letters*, vol. 23, no. 19, pp. 1026–1028, 1987. DOI: 10.1049/el:19870719.

[11] F. Kish, R. Nagarajan, D. Welch, P. Evans, J. Rossi, J. Pleumeekers, A. Dentai, M. Kato, S. Corzine, R. Muthiah, M. Ziari, R. Schneider, M. Reffle, T. Butrie, D. Lambert, M. Missey, V. Lal, M. Fisher, S. Murthy, R. Salvatore, S. Demars, A. James, and C. Joyner, "From visible light-emitting diodes to large-scale III-V photonic integrated circuits", *Proceedings of the IEEE*, vol. 101, no. 10, pp. 2255–2270, 2013. DOI: 10.1109/JPROC.2013.2275018.

[12] J. Summers, T. Vallaitis, P. Evans, M. Ziari, P. Studenkov, M. Fisher, J. Sena, A. James, S. Corzine, D. Pavinski, J. Ou-Yang, M. Missey, D. Gold, W. Williams, M. Lai, D. Welch, and F. Kish, "Monolithic InP-based coherent transmitter photonic integrated circuit with 2.25 Tbit/s capacity", *Electronics Letters*, vol. 50, no. 16, pp. 1150–1152, 2014. DOI: 10.1049/el.2014.2011.

[13] W. D. Sacher, Z. Yong, J. C. Mikkelsen, A. Bois, Y. Yang, J. C. Mak, P. Dumais, D. Goodwill, C. Ma, J. Jeong, E. Bernier, and J. K. Poon, "Multilayer silicon nitride-on-silicon integrated photonic platform for 3D photonic circuits", in *Conference on Lasers and Electro-Optics*, Washington, D.C.: OSA, 2016, JTh4C.3. DOI: 10.1364/CLEO_AT.2016.JTh4C.3.

[14] L. E. Hargrove, R. L. Fork, and M. A. Pollack, "Locking of He–Ne laser modes induced by synchronous intracavity modulation", *Applied Physics Letters*, vol. 5, no. 1, pp. 4–5, 1964. DOI: 10.1063/1.1754025.

[15] J. N. Eckstein, A. I. Ferguson, and T. W. Hänsch, "High-resolution two-photon spectroscopy with picosecond light pulses", *Physical Review Letters*, vol. 40, no. 13, pp. 847–850, 1978. DOI: 10.1103/PhysRevLett.40.847.

[16] T. Kobayashi, T. Sueta, Y. Cho, and Y. Matsuo, "High-repetition-rate optical pulse generator using a Fabry-Perot electro-optic modulator", *Applied Physics Letters*, vol. 21, no. 8, pp. 341–343, 1972. DOI: 10.1063/1.1654403.

[17] H. Takara, T. Ohara, K. Mori, K.-I. Sato, E. Yamada, Y. Inoue, T. Shibata, M. Abe, T. Morioka, and K.-I. Sato, "More than 1000 channel optical frequency chain generation from single supercontinuum source with 12.5 GHz channel spacing", *Electronics Letters*, vol. 36, no. 25, pp. 2089–2090, 2000. DOI: 10.1049/el:20001461.

[18] T. Ohara, H. Takara, T. Yamamoto, H. Masuda, T. Morioka, M. Abe, and H. Takahashi, "Over-1000-channel ultradense WDM transmission with supercontinuum multicarrier source", *Journal of Lightwave Technology*, vol. 24, no. 6, pp. 2311–2317, 2006. DOI: 10.1109/JLT.2006.874548.

[19] A. H. Gnauck, B. P. P. Kuo, E. Myslivets, R. M. Jopson, M. Dinu, J. E. Simsarian, P. J. Winzer, and S. Radic, "Comb-based 16-QAM transmitter spanning the C and L bands", *IEEE Photonics Technology Letters*, vol. 26, no. 8, pp. 821–824, 2014. DOI: 10.1109/LPT.2014.2306989.

[20] B. J. Puttnam, R. S. Luis, W. Klaus, J. Sakaguchi, J.-M. Delgado Mendinueta, Y. Awaji, N. Wada, Y. Tamura, T. Hayashi, M. Hirano, and J. Marciante, "2.15 Pb/s transmission using a 22 core homogeneous single-mode multi-core fiber and wideband optical comb", in *2015 European Conference on Optical Communication (ECOC)*, vol. 2015-Novem, IEEE, 2015, pp. 1–3. DOI: 10.1109/ECOC.2015.7341685.

[21] M. Mazur, A. Lorences-Riesgo, J. Schroder, P. A. Andrekson, and M. Karlsson, "High spectral efficiency PM-128QAM comb-based superchannel transmission enabled by a single shared optical pilot tone", *Journal of Lightwave Technology*, vol. 36, no. 6, pp. 1318–1325, 2018. DOI: 10.1109/JLT.2017.2786750.

[22] T. J. Kippenberg, S. M. Spillane, and K. J. Vahala, "Kerr-nonlinearity optical parametric oscillation in an ultrahigh-Q toroid microcavity", *Physical Review Letters*, vol. 93, no. 8, pp. 18–21, 2004. DOI: 10.1103/PhysRevLett.93.083904.

[23] P. Del'Haye, A. Schliesser, O. Arcizet, T. Wilken, R. Holzwarth, and T. J. Kippenberg, "Optical frequency comb generation from a monolithic microresonator", *Nature*, vol. 450, no. 7173, pp. 1214–1217, 2007. DOI: 10.1038/nature06401.

[24] J. S. Levy, A. Gondarenko, M. a. Foster, A. C. Turner-Foster, A. L. Gaeta, and M. Lipson, "CMOS-compatible multiple-wavelength oscillator for on-chip optical interconnects", *Nature Photonics*, vol. 4, no. 1, pp. 37–40, 2010. DOI: 10.1038/nphoton.2009.259.

[25] J. Pfeifle, V. Brasch, M. Lauermann, Y. Yu, D. Wegner, T. Herr, K. Hartinger, P. Schindler, J. Li, D. Hillerkuss, R. Schmogrow, C. Weimann, R. Holzwarth, W. Freude, J. Leuthold, T. J. Kippenberg, and C. Koos, "Coherent terabit communications with microresonator Kerr frequency combs", *Nature Photonics*, vol. 8, no. 5, pp. 375–380, 2014. DOI: 10.1038/nphoton.2014.57.

[26] J. Pfeifle, A. Coillet, R. Henriet, K. Saleh, P. Schindler, C. Weimann, W. Freude, I. V. Balakireva, L. Larger, C. Koos, and Y. K. Chembo, "Optimally coherent Kerr combs generated with crystalline whispering-gallery-mode resonators for ultrahigh capacity fiber communications", *Physical Review Letters*, vol. 114, no. 9, p. 093 902, 2015. DOI: 10.1103/PhysRevLett.114.093902.

[27] P. Marin-Palomo, J. N. Kemal, M. Karpov, A. Kordts, J. Pfeifle, M. H. P. Pfeiffer, P. Trocha, S. Wolf, V. Brasch, M. H. Anderson, R. Rosenberger, K. Vijayan, W. Freude, T. J. Kippenberg, and C. Koos, "Microresonator-based solitons for massively parallel coherent optical communications", *Nature*, vol. 546, no. 7657, pp. 274–279, 2017. DOI: 10.1038/nature22387.

[28] X. Xue, P.-h. Wang, Y. Xuan, M. Qi, and A. M. Weiner, "Microresonator Kerr frequency combs with high conversion efficiency", *Laser & Photonics Reviews*, vol. 11, no. 1, p. 1 600 276, 2017. DOI: 10.1002/lpor.201600276.

[29] Keang-Po Ho and Han-Wei Cuei, "Generation of arbitrary quadrature signals using one dual-drive modulator", *Journal of Lightwave Technology*, vol. 23, no. 2, pp. 764–770, 2005. DOI: 10.1109/JLT.2004.838855.

[30] C. E. Shannon, "A mathematical theory of communication", *Bell System Technical Journal*, vol. 27, no. 4, pp. 623–656, 1948. DOI: 10.1002/j.1538-7305.1948.tb00917.x.

[31] G. P. Agrawal, "Loss management", in *Fiber-Optic Communication Systems*, Fourth Edi, Hoboken, NJ, USA: John Wiley & Sons, Inc., 2011, ch. 7, pp. 295–344. DOI: 10.1002/9780470918524.ch7.

[32] E. Ip, A. P. T. Lau, D. J. F. Barros, and J. M. Kahn, "Coherent detection in optical fiber systems", *Optics Express*, vol. 16, no. 2, pp. 753–791, 2008. DOI: 10.1364/OE.16.000753.

[33] G. Agrawal, "Pulse propagation in fibers", in *Nonlinear Fiber Optics*, 5th ed., Elsevier, 2013, ch. 2, pp. 27–56. DOI: 10.1016/B978-0-12-397023-7.00002-4.

[34] A. Carena, G. Bosco, V. Curri, P. Poggiolini, M. T. Taiba, and F. Forghieri, "Statistical characterization of PM-QPSK signals after propagation in uncompensated fiber links", in *36th European Conference and Exhibition on Optical Communication*, IEEE, 2010, P4.07. DOI: 10.1109/ECOC.2010.5621509.

[35] A. Splett, C. Kurtzke, and K. Petermann, "Ultimate transmission capacity of amplified optical fiber communication systems taking into

account fiber nonlinearities", in *European Conference on Optical Communication*, 1993, MoC2.4.

[36] P. Poggiolini, A. Carena, V. Curri, G. Bosco, and F. Forghieri, "Analytical modeling of nonlinear propagation in uncompensated optical transmission links", *IEEE Photonics Technology Letters*, vol. 23, no. 11, pp. 742–744, 2011. DOI: 10.1109/LPT.2011.2131125.

[37] H. Zhang, J.-X. Cai, H. G. Batshon, C. R. Davidson, Y. Sun, M. Mazurczyk, D. G. Foursa, A. Pilipetskii, G. Mohs, and N. S. Bergano, "16QAM transmission with 5.2 bits/s/Hz spectral efficiency over transoceanic distance", *Optics Express*, vol. 20, no. 11, pp. 11 688–11 693, 2012. DOI: 10.1364/OE.20.011688.

[38] D. Ofelt and G. Nicholl. (2013). BER objective for 400GE, [Online]. Available: http://www.ieee802.org/3/400GSG/public/13_07/ofelt_400_01_0713.pdf (visited on 02/08/2018).

[39] L. M. Zhang and F. R. Kschischang, "Staircase codes with 6% to 33% overhead", *Journal of Lightwave Technology*, vol. 32, no. 10, pp. 1999–2002, 2014. DOI: 10.1109/JLT.2014.2316732.

[40] K. Kikuchi, T. Okoshi, M. Nagamatsu, and N. Henmi, "Degradation of bit-error rate in coherent optical communications due to spectral spread of the transmitter and the local oscillator", *Journal of Lightwave Technology*, vol. 2, no. 6, pp. 1024–1033, 1984. DOI: 10.1109/JLT.1984.1073700.

[41] G. Foschini and G. Vannucci, "Characterizing filtered light waves corrupted by phase noise", *IEEE Transactions on Information Theory*, vol. 34, no. 6, pp. 1437–1448, 1988. DOI: 10.1109/18.21283.

[42] T. Pfau, S. Hoffmann, and R. Noe, "Hardware-efficient coherent digital receiver concept with feedforward carrier recovery for M-QAM constellations", *Journal of Lightwave Technology*, vol. 27, no. 8, pp. 989–999, 2009. DOI: 10.1109/JLT.2008.2010511.

[43] K. Petermann, "Noise characteristics of solitary laser diodes", in *Laser Diode Modulation and Noise*, 1988, ch. 7, pp. 152–213.

[44] K. Kikuchi, "Characterization of semiconductor-laser phase noise and estimation of bit-error rate performance with low-speed offline digital coherent receivers", *Optics Express*, vol. 20, no. 5, pp. 5291–5302, 2012. DOI: 10.1364/OE.20.005291.

[45] A. Kakkar, J. Rodrigo Navarro, R. Schatz, X. Pang, O. Ozolins, A. Udalcovs, H. Louchet, S. Popov, and G. Jacobsen, "Laser frequency noise in coherent optical systems: Spectral regimes and impairments",

Scientific Reports, vol. 7, no. 1, p. 844, 2017. DOI: 10.1038/s41598-017-00868-4.

[46] Z. Tong, A. O. J. Wiberg, E. Myslivets, B. P. P. Kuo, N. Alic, and S. Radic, "Spectral linewidth preservation in parametric frequency combs seeded by dual pumps", *Optics Express*, vol. 20, no. 16, pp. 17 610–17 619, 2012. DOI: 10.1364/OE.20.017610.

[47] A. Ishizawa, T. Nishikawa, A. Mizutori, H. Takara, A. Takada, T. Sogawa, and M. Koga, "Phase-noise characteristics of a 25-GHz-spaced optical frequency comb based on a phase- and intensity-modulated laser", *Optics Express*, vol. 21, no. 24, pp. 29 186–29 194, 2013. DOI: 10.1364/OE.21.029186.

[48] A. J. Metcalf, V. Torres-Company, D. E. Leaird, and A. M. Weiner, "High-power broadly tunable electrooptic frequency comb generator", *IEEE Journal on Selected Topics in Quantum Electronics*, vol. 19, no. 6, 2013. DOI: 10.1109/JSTQE.2013.2268384.

[49] R. R. Alfano and S. L. Shapiro, "Observation of self-phase modulation and small-scale filaments in crystals and glasses", *Physical Review Letters*, vol. 24, no. 11, pp. 592–594, 1970. DOI: 10.1103/PhysRevLett.24.592.

[50] J. K. Ranka, R. S. Windeler, and A. J. Stentz, "Visible continuum generation in air–silica microstructure optical fibers with anomalous dispersion at 800 nm", *Optics Letters*, vol. 25, no. 1, pp. 25–27, 2000. DOI: 10.1364/OL.25.000025.

[51] D. J. Jones, S. A. Diddams, J. K. Ranka, A. Stentz, R. S. Windeler, J. L. Hall, and S. T. Cundiff, "Carrier-envelope phase control of femtosecond mode-locked lasers and direct optical frequency synthesis", *Science*, vol. 288, no. 5466, pp. 635–639, 2000. DOI: 10.1126/science.288.5466.635.

[52] T. R. Schibli, K. Minoshima, F.-L. Hong, H. Inaba, A. Onae, H. Matsumoto, I. Hartl, and M. E. Fermann, "Frequency metrology with a turnkey all-fiber system", *Optics Letters*, vol. 29, no. 21, pp. 2467–2469, 2004. DOI: 10.1364/OL.29.002467.

[53] L. C. Sinclair, J.-D. Deschênes, L. Sonderhouse, W. C. Swann, I. H. Khader, E. Baumann, N. R. Newbury, and I. Coddington, "Invited article: A compact optically coherent fiber frequency comb", *Review of Scientific Instruments*, vol. 86, no. 8, p. 081 301, 2015. DOI: 10.1063/1.4928163.

[54] D. C. Cole, K. Beha, F. N. Baynes, P. Del'Haye, A. Rolland, T. M. Fortier, F. Quinlan, S. Diddams, and S. B. Papp, "Self-referencing a

10 GHz electro-optic comb", in *CLEO: 2015*, Washington, D.C.: OSA, 2015, STh4N.5. DOI: 10.1364/CLEO_SI.2015.STh4N.5.

[55] K. Beha, D. C. Cole, P. Del'Haye, A. Coillet, S. A. Diddams, and S. B. Papp, "Electronic synthesis of light", *Optica*, vol. 4, no. 4, pp. 406–411, 2017. DOI: 10.1364/OPTICA.4.000406.

[56] E. S. Lamb, D. R. Carlson, D. D. Hickstein, J. R. Stone, S. A. Diddams, and S. B. Papp, "Optical-frequency measurements with a Kerr microcomb and photonic-chip supercontinuum", *Physical Review Applied*, vol. 9, no. 2, p. 024 030, 2018. DOI: 10.1103/PhysRevApplied.9.024030.

[57] T. Udem, J. Reichert, R. Holzwarth, and T. W. Hänsch, "Absolute optical frequency measurement of the Cesium D_1 line with a mode-locked laser", *Physical Review Letters*, vol. 82, no. 18, pp. 3568–3571, 1999. DOI: 10.1103/PhysRevLett.82.3568.

[58] S. A. Diddams, D. J. Jones, J. Ye, S. T. Cundiff, J. L. Hall, J. K. Ranka, R. S. Windeler, R. Holzwarth, T. Udem, and T. W. Hänsch, "Direct link between microwave and optical frequencies with a 300 THz femtosecond laser comb", *Physical Review Letters*, vol. 84, no. 22, pp. 5102–5105, 2000. DOI: 10.1103/PhysRevLett.84.5102.

[59] R. Holzwarth, T. Udem, T. W. Hänsch, J. C. Knight, W. J. Wadsworth, and P. S. J. Russell, "Optical frequency synthesizer for precision spectroscopy", *Physical Review Letters*, vol. 85, no. 11, pp. 2264–2267, 2000. DOI: 10.1103/PhysRevLett.85.2264.

[60] T. Udem, R. Holzwarth, and T. W. Hänsch, "Optical frequency metrology", *Nature*, vol. 416, no. 6877, pp. 233–237, 2002. DOI: 10.1038/416233a.

[61] S. T. Cundiff and J. Ye, "Colloquium : Femtosecond optical frequency combs", *Reviews of Modern Physics*, vol. 75, no. 1, pp. 325–342, 2003. DOI: 10.1103/RevModPhys.75.325.

[62] S. A. Diddams, L. Hollberg, and V. Mbele, "Molecular fingerprinting with the resolved modes of a femtosecond laser frequency comb", *Nature*, vol. 445, no. 7128, pp. 627–630, 2007. DOI: 10.1038/nature05524.

[63] T. Ideguchi, S. Holzner, B. Bernhardt, G. Guelachvili, N. Picqué, and T. W. Hänsch, "Coherent Raman spectro-imaging with laser frequency combs", *Nature*, vol. 502, no. 7471, pp. 355–358, 2013. DOI: 10.1038/nature12607.

[64] A. Foltynowicz, T. Ban, P. Masłowski, F. Adler, and J. Ye, "Quantum-noise-limited optical frequency comb spectroscopy", *Physical Review*

Letters, vol. 107, no. 23, p. 233 002, 2011. DOI: 10.1103/PhysRevLett.107.233002.

[65] A. L. Wolf, J. Morgenweg, J. C. J. Koelemeij, S. A. van den Berg, W. Ubachs, and K. S. E. Eikema, "Direct frequency-comb spectroscopy of a dipole-forbidden clock transition in trapped $^{40}Ca^{+}$ ions", *Optics Letters*, vol. 36, no. 1, pp. 49–51, 2011. DOI: 10.1364/OL.36.000049.

[66] T. Steinmetz, T. Wilken, C. Araujo-Hauck, R. Holzwarth, T. W. Hansch, L. Pasquini, A. Manescau, S. D'Odorico, M. T. Murphy, T. Kentischer, W. Schmidt, and T. Udem, "Laser frequency combs for astronomical observations", *Science*, vol. 321, no. 5894, pp. 1335–1337, 2008. DOI: 10.1126/science.1161030.

[67] X. Yi, K. Vahala, J. Li, S. Diddams, G. Ycas, P. Plavchan, S. Leifer, J. Sandhu, G. Vasisht, P. Chen, P. Gao, J. Gagne, E. Furlan, M. Bottom, E. C. Martin, M. P. Fitzgerald, G. Doppmann, and C. Beichman, "Demonstration of a near-IR line-referenced electro-optical laser frequency comb for precision radial velocity measurements in astronomy", *Nature Communications*, vol. 7, p. 10 436, 2016. DOI: 10.1038/ncomms10436.

[68] M. T. Hassan, T. T. Luu, A. Moulet, O. Raskazovskaya, P. Zhokhov, M. Garg, N. Karpowicz, a. M. Zheltikov, V. Pervak, F. Krausz, and E. Goulielmakis, "Optical attosecond pulses and tracking the nonlinear response of bound electrons", *Nature*, vol. 530, no. 7588, pp. 66–70, 2016. DOI: 10.1038/nature16528.

[69] I. Coddington, W. Swann, and N. Newbury, "Coherent multiheterodyne spectroscopy using stabilized optical frequency combs", *Physical Review Letters*, vol. 100, no. 1, p. 013 902, 2008. DOI: 10.1103/PhysRevLett.100.013902.

[70] G. Millot, S. Pitois, M. Yan, T. Hovhannisyan, A. Bendahmane, T. W. Hänsch, and N. Picqué, "Frequency-agile dual-comb spectroscopy", *Nature Photonics*, vol. 10, no. 1, pp. 27–30, 2016. DOI: 10.1038/nphoton.2015.250.

[71] I. Coddington, N. Newbury, and W. Swann, "Dual-comb spectroscopy", *Optica*, vol. 3, no. 4, pp. 414–426, 2016. DOI: 10.1364/OPTICA.3.000414.

[72] V. Durán, S. Tainta, and V. Torres-Company, "Ultrafast electrooptic dual-comb interferometry", *Optics Express*, vol. 23, no. 23, pp. 30 557–30 569, 2015. DOI: 10.1364/OE.23.030557.

[73] M.-G. Suh, Q.-F. Yang, K. Y. Yang, X. Yi, and K. J. Vahala, "Microresonator soliton dual-comb spectroscopy", *Science*, vol. 354, no. 6312, pp. 600–603, 2016. DOI: 10.1126/science.aah6516.

[74] J. Lee, Y.-J. Kim, K. Lee, S. Lee, and S.-W. Kim, "Time-of-flight measurement with femtosecond light pulses", *Nature Photonics*, vol. 4, no. 10, pp. 716–720, 2010. DOI: 10.1038/nphoton.2010.175.

[75] N. Schuhler, Y. Salvadé, S. Lévêque, R. Dändliker, and R. Holzwarth, "Frequency-comb-referenced two-wavelength source for absolute distance measurement", *Optics Letters*, vol. 31, no. 21, pp. 3101–3103, 2006. DOI: 10.1364/OL.31.003101.

[76] I. Coddington, W. C. Swann, L. Nenadovic, and N. R. Newbury, "Rapid and precise absolute distance measurements at long range", *Nature Photonics*, vol. 3, no. 6, pp. 351–356, 2009. DOI: 10.1038/nphoton.2009.94.

[77] J. McFerran, E. Ivanov, A. Bartels, G. Wilpers, C. Oates, S. Diddams, and L. Hollberg, "Low-noise synthesis of microwave signals from an optical source", *Electronics Letters*, vol. 41, no. 11, pp. 650–651, 2005. DOI: 10.1049/el:20050505.

[78] T. M. Fortier, M. S. Kirchner, F. Quinlan, J. Taylor, J. C. Bergquist, T. Rosenband, N. Lemke, A. Ludlow, Y. Jiang, C. W. Oates, and S. A. Diddams, "Generation of ultrastable microwaves via optical frequency division", *Nature Photonics*, vol. 5, no. 7, pp. 425–429, 2011. DOI: 10.1038/nphoton.2011.121.

[79] J. Li, X. Yi, H. Lee, S. A. Diddams, and K. J. Vahala, "Electro-optical frequency division and stable microwave synthesis", *Science*, vol. 345, no. 6194, pp. 309–313, 2014. DOI: 10.1126/science.1252909.

[80] W. Liang, D. Eliyahu, V. S. Ilchenko, A. A. Savchenkov, A. B. Matsko, D. Seidel, and L. Maleki, "High spectral purity Kerr frequency comb radio frequency photonic oscillator", *Nature Communications*, vol. 6, no. 1, p. 7957, 2015. DOI: 10.1038/ncomms8957.

[81] C.-B. Huang, Z. Jiang, D. Leaird, J. Caraquitena, and A. Weiner, "Spectral line-by-line shaping for optical and microwave arbitrary waveform generations", *Laser & Photonics Review*, vol. 2, no. 4, pp. 227–248, 2008. DOI: 10.1002/lpor.200810001.

[82] S. T. Cundiff and A. M. Weiner, "Optical arbitrary waveform generation", *Nature Photonics*, vol. 4, no. 11, pp. 760–766, 2010. DOI: 10.1038/nphoton.2010.196.

[83] R. Slavik, S. G. Farwell, M. J. Wale, and D. J. Richardson, "Compact optical comb generator using InP tunable laser and push-pull modula-

tor", *IEEE Photonics Technology Letters*, vol. 27, no. 2, pp. 217–220, 2015. DOI: 10.1109/LPT.2014.2365259.

[84] V. Corral, R. Guzmán, C. Gordón, X. J. M. Leijtens, and G. Carpintero, "Optical frequency comb generator based on a monolithically integrated passive mode-locked ring laser with a Mach-Zehnder interferometer", *Optics Letters*, vol. 41, no. 9, pp. 1937–1940, 2016. DOI: 10.1364/OL.41.001937.

[85] F. Lelarge, B. Dagens, J. Renaudier, R. Brenot, A. Accard, F. van Dijk, D. Make, O. L. Gouezigou, J.-G. Provost, F. Poingt, J. Landreau, O. Drisse, E. Derouin, B. Rousseau, F. Pommereau, and G.-H. Duan, "Recent advances on InAs/InP quantum dash based semiconductor lasers and optical amplifiers operating at 1.55 µm", *IEEE Journal of Selected Topics in Quantum Electronics*, vol. 13, no. 1, pp. 111–124, 2007. DOI: 10.1109/JSTQE.2006.887154.

[86] T. J. Kippenberg, R. Holzwarth, and S. A. Diddams, "Microresonator-based optical frequency combs", *Science*, vol. 332, no. 6029, pp. 555–559, 2011. DOI: 10.1126/science.1193968.

[87] Y. Okawachi, K. Saha, J. S. Levy, Y. H. Wen, M. Lipson, and A. L. Gaeta, "Octave-spanning frequency comb generation in a silicon nitride chip", *Optics Letters*, vol. 36, no. 17, pp. 3398–3400, 2011. DOI: 10.1364/OL.36.003398.

[88] F. Ferdous, H. Miao, D. E. Leaird, K. Srinivasan, J. Wang, L. Chen, L. T. Varghese, and A. M. Weiner, "Spectral line-by-line pulse shaping of on-chip microresonator frequency combs", *Nature Photonics*, vol. 5, no. 12, pp. 770–776, 2011. DOI: 10.1038/nphoton.2011.255.

[89] T. Herr, V. Brasch, J. D. Jost, C. Y. Wang, N. M. Kondratiev, M. L. Gorodetsky, and T. J. Kippenberg, "Temporal solitons in optical microresonators", *Nature Photonics*, vol. 8, no. 2, pp. 145–152, 2014. DOI: 10.1038/nphoton.2013.343.

[90] T. Herr, K. Hartinger, J. Riemensberger, C. Y. Wang, E. Gavartin, R. Holzwarth, M. L. Gorodetsky, and T. J. Kippenberg, "Universal formation dynamics and noise of Kerr-frequency combs in microresonators", *Nature Photonics*, vol. 6, no. 7, pp. 480–487, 2012. DOI: 10.1038/nphoton.2012.127.

[91] X. Xue, Y. Xuan, Y. Liu, P.-H. Wang, S. Chen, J. Wang, D. E. Leaird, M. Qi, and A. M. Weiner, "Mode-locked dark pulse Kerr combs in normal-dispersion microresonators", *Nature Photonics*, vol. 9, no. 9, pp. 594–600, 2015. DOI: 10.1038/nphoton.2015.137.

[92] J. Veselka and S. Korotky, "A multiwavelength source having precise channel spacing for WDM systems", *IEEE Photonics Technology Letters*, vol. 10, no. 7, pp. 958–960, 1998. DOI: 10.1109/68.681283.

[93] B. P. Kuo, E. Myslivets, V. Ataie, E. G. Temprana, N. Alic, and S. Radic, "Wideband parametric frequency comb as coherent optical carrier", *Journal of Lightwave Technology*, vol. 31, no. 21, pp. 3414–3419, 2013. DOI: 10.1109/JLT.2013.2279540.

[94] E. Temprana, V. Ataie, B. P.-P. Kuo, E. Myslivets, N. Alic, and S. Radic, "Low-noise parametric frequency comb for continuous C-plus-L-band 16-QAM channels generation", *Optics Express*, vol. 22, no. 6, pp. 6822–6828, 2014. DOI: 10.1364/OE.22.006822.

[95] R. Wu, V. Torres-Company, D. E. Leaird, and A. M. Weiner, "Supercontinuum-based 10-GHz flat-topped optical frequency comb generation", *Optics Express*, vol. 21, no. 5, pp. 6045–6052, 2013. DOI: 10.1364/OE.21.006045.

[96] V. Ataie, E. Temprana, L. Liu, E. Myslivets, B. P.-P. Kuo, N. Alic, and S. Radic, "Ultrahigh count coherent WDM channels transmission using optical parametric comb-based frequency synthesizer", *Journal of Lightwave Technology*, vol. 33, no. 3, pp. 694–699, 2015. DOI: 10.1109/JLT.2015.2388579.

[97] E. Temprana, B.-P. Kuo, N. Alic, S. Radic, and S. Grubb, "400 Gb/s WDM DP-256-QAM transmission with 50 GHz channel separation", in *2016 IEEE Photonics Conference (IPC)*, IEEE, 2016. DOI: 10.1109/IPCon.2016.7830949.

[98] E. Temprana, E. Myslivets, B. P.-. P. Kuo, L. Liu, V. Ataie, N. Alic, and S. Radic, "Overcoming Kerr-induced capacity limit in optical fiber transmission", *Science*, vol. 348, no. 6242, pp. 1445–1448, 2015. DOI: 10.1126/science.aab1781.

[99] R. Dar and P. J. Winzer, "On the limits of digital back-propagation in fully loaded WDM systems", *IEEE Photonics Technology Letters*, vol. 28, no. 11, pp. 1253–1256, 2016. DOI: 10.1109/LPT.2016.2522969.

[100] J.-X. Cai, H. Zhang, H. G. Batshon, M. Mazurczyk, O. V. Sinkin, D. G. Foursa, A. N. Pilipetskii, G. Mohs, and N. S. Bergano, "200 Gb/s and dual wavelength 400 Gb/s transmission over transpacific distance at 6.0 b/s/Hz spectral efficiency", *Journal of Lightwave Technology*, vol. 32, no. 4, pp. 832–839, 2014. DOI: 10.1109/JLT.2013.2284669.

[101] E. Temprana, E. Myslivets, L. Liu, V. Ataie, A. Wiberg, B. Kuo, N. Alic, and S. Radic, "Two-fold transmission reach enhancement enabled by transmitter-side digital backpropagation and optical frequency comb-

derived information carriers", *Optics Express*, vol. 23, no. 16, pp. 20 774–20 783, 2015. DOI: 10.1364/OE.23.020774.

[102] E. Temprana, E. Myslivets, V. Ataie, B.-P. Kuo, N. Alic, V. Vusirikala, V. Dangui, and S. Radic, "Demonstration of coherent transmission reach tripling by frequency-referenced nonlinearity pre-compensation in EDFA-only SMF link", in *ECOC 2016; 42nd European Conference on Optical Communication*, 2016, pp. 376–378.

[103] R. Maher, T. Xu, L. Galdino, M. Sato, A. Alvarado, K. Shi, S. J. Savory, B. C. Thomsen, R. I. Killey, and P. Bayvel, "Spectrally shaped DP-16QAM super-channel transmission with multi-channel digital back-propagation.", *Scientific reports*, vol. 5, p. 8214, 2015. DOI: 10.1038/srep08214.

[104] D. S. Millar, R. Maher, D. Lavery, T. Koike-Akino, M. Pajovic, A. Alvarado, M. Paskov, K. Kojima, K. Parsons, B. C. Thomsen, S. J. Savory, and P. Bayvel, "Design of a 1 Tb/s superchannel coherent receiver", *Journal of Lightwave Technology*, vol. 34, no. 6, pp. 1453–1463, 2016. DOI: 10.1109/JLT.2016.2519260.

[105] L. Lundberg, M. Mazur, A. Lorences-Riesgo, M. Karlsson, and P. A. Andrekson, "Joint carrier recovery for DSP complexity reduction in frequency comb-based superchannel transceivers", *European Conference on Optical Communication*, Th1D, 2017.

[106] G.-H. Duan, A. Shen, A. Akrout, F. V. Dijk, F. Lelarge, F. Pommereau, O. LeGouezigou, J.-G. Provost, H. Gariah, F. Blache, F. Mallecot, K. Merghem, A. Martinez, and A. Ramdane, "High performance InP-based quantum dash semiconductor mode-locked lasers for optical communications", *Bell Labs Technical Journal*, vol. 14, no. 3, pp. 63–84, 2009. DOI: 10.1002/bltj.20388.

[107] P.-H. Wang, F. Ferdous, H. Miao, J. Wang, D. E. Leaird, K. Srinivasan, L. Chen, V. Aksyuk, and A. M. Weiner, "Observation of correlation between route to formation, coherence, noise, and communication performance of Kerr combs", *Optics Express*, vol. 20, no. 28, pp. 29 284–29 295, 2012. DOI: 10.1364/OE.20.029284.

[108] J. S. Levy, K. Saha, Y. Okawachi, M. A. Foster, A. L. Gaeta, and M. Lipson, "High-performance silicon-nitride-based multiple-wavelength source", *IEEE Photonics Technology Letters*, vol. 24, no. 16, pp. 1375–1377, 2012. DOI: 10.1109/LPT.2012.2204245.

[109] V. Vujicic, A. Anthur, V. Panapakkam, R. Zhou, Q. Gaimard, K. Merghem, F. Lelarge, A. Ramdane, and L. Barry, "Tbit/s optical interconnects based on low linewidth quantum-dash lasers and coherent

detection", in *Conference on Lasers and Electro-Optics*, vol. 1, Washington, D.C.: OSA, 2016, SF2F.4. DOI: 10.1364/CLEO_SI.2016.SF2F.4.

[110] J. N. Kemal, P. Marin-Palomo, K. Merghem, A. Guy, C. Calo, R. Brenot, F. Lelarge, A. Ramdane, S. Randel, W. Freude, and C. Koos, "32QAM WDM transmission using a quantum-dash passively mode-locked laser with resonant feedback", in *Optical Fiber Communication Conference Postdeadline Papers*, Washington, D.C.: OSA, 2017, Th5C.3. DOI: 10.1364/OFC.2017.Th5C.3.

[111] C. Weimann, P. C. Schindler, R. Palmer, S. Wolf, D. Bekele, D. Korn, J. Pfeifle, S. Koeber, R. Schmogrow, L. Alloatti, D. Elder, H. Yu, W. Bogaerts, L. R. Dalton, W. Freude, J. Leuthold, and C. Koos, "Silicon-organic hybrid (SOH) frequency comb sources for terabit/s data transmission", *Optics Express*, vol. 22, no. 3, pp. 3629–3637, 2014. DOI: 10.1364/OE.22.003629.

[112] K. J. Vahala, "Optical microcavities", *Nature*, vol. 424, no. 6950, pp. 839–846, 2003. DOI: 10.1038/nature01939.

[113] B. Little, S. Chu, H. Haus, J. Foresi, and J.-P. Laine, "Microring resonator channel dropping filters", *Journal of Lightwave Technology*, vol. 15, no. 6, pp. 998–1005, 1997. DOI: 10.1109/50.588673.

[114] J. E. Heebner and R. W. Boyd, "Enhanced all-optical switching by use of a nonlinear fiber ring resonator", *Optics Letters*, vol. 24, no. 12, pp. 847–849, 1999. DOI: 10.1364/OL.24.000847.

[115] A. Yariv, "Universal relations for coupling of optical power between microresonators and dielectric waveguides", *Electronics Letters*, vol. 36, no. 4, pp. 321–322, 2000. DOI: 10.1049/el:20000340.

[116] W. Bogaerts, P. De Heyn, T. Van Vaerenbergh, K. De Vos, S. Kumar Selvaraja, T. Claes, P. Dumon, P. Bienstman, D. Van Thourhout, and R. Baets, "Silicon microring resonators", *Laser & Photonics Reviews*, vol. 6, no. 1, pp. 47–73, 2012. DOI: 10.1002/lpor.201100017.

[117] W.-P. Huang, "Coupled-mode theory for optical waveguides: An overview", *Journal of the Optical Society of America A*, vol. 11, no. 3, pp. 963–983, 1994. DOI: 10.1364/JOSAA.11.000963.

[118] M. Chin and S. Ho, "Design and modeling of waveguide-coupled single-mode microring resonators", *Journal of Lightwave Technology*, vol. 16, no. 8, pp. 1433–1446, 1998. DOI: 10.1109/50.704609.

[119] V. P. Tzolov, N. Godbout, S. Lacroix, and M. Fontaine, "Nonlinear self-phase-modulation effects: A vectorial first-order perturbation approach", *Optics Letters*, vol. 20, no. 5, pp. 456–458, 1995. DOI: 10.1364/OL.20.000456.

[120] K. Ikeda, "Multiple-valued stationary state and its instability of the transmitted light by a ring cavity system", *Optics Communications*, vol. 30, no. 2, pp. 257–261, 1979. DOI: 10.1016/0030-4018(79)90090-7.

[121] V. Torres-Company, D. Castelló-Lurbe, and E. Silvestre, "Comparative analysis of spectral coherence in microresonator frequency combs", *Optics Express*, vol. 22, no. 4, pp. 4678–4691, 2014. DOI: 10.1364/OE.22.004678.

[122] T. Hansson and S. Wabnitz, "Frequency comb generation beyond the Lugiato-Lefever equation: Multi-stability and super cavity solitons", *Journal of the Optical Society of America B*, vol. 32, no. 7, pp. 1259–1266, 2015. DOI: 10.1364/JOSAB.32.001259.

[123] L. Lugiato and R. Lefever, "Spatial dissipative structures in passive optical systems", *Physical Review Letters*, vol. 58, no. 21, pp. 2209–2211, 1987. DOI: 10.1103/PhysRevLett.58.2209.

[124] S. Coen, H. G. Randle, T. Sylvestre, and M. Erkintalo, "Modeling of octave-spanning Kerr frequency combs using a generalized mean-field Lugiato-Lefever model", *Optics Letters*, vol. 38, no. 1, pp. 37–39, 2013. DOI: 10.1364/OL.38.000037.

[125] M. Haelterman, S. Trillo, and S. Wabnitz, "Dissipative modulation instability in a nonlinear dispersive ring cavity", *Optics Communications*, vol. 91, no. 5-6, pp. 401–407, 1992. DOI: 10.1016/0030-4018(92)90367-Z.

[126] A. Scroggie, W. Firth, G. McDonald, M. Tlidi, R. Lefever, and L. Lugiato, "Pattern formation in a passive Kerr cavity", *Chaos, Solitons & Fractals*, vol. 4, no. 8-9, pp. 1323–1354, 1994. DOI: 10.1016/0960-0779(94)90084-1.

[127] Y. K. Chembo and C. R. Menyuk, "Spatiotemporal Lugiato-Lefever formalism for Kerr-comb generation in whispering-gallery-mode resonators", *Physical Review A*, vol. 87, no. 5, p. 053 852, 2013. DOI: 10.1103/PhysRevA.87.053852.

[128] C. Bao, L. Zhang, A. Matsko, Y. Yan, Z. Zhao, G. Xie, A. M. Agarwal, L. C. Kimerling, J. Michel, L. Maleki, and A. E. Willner, "Nonlinear conversion efficiency in Kerr frequency comb generation", *Optics Letters*, vol. 39, no. 21, pp. 6126–6129, 2014. DOI: 10.1364/OL.39.006126.

[129] C. Milián, A. V. Gorbach, M. Taki, A. V. Yulin, and D. V. Skryabin, "Solitons and frequency combs in silica microring resonators: Interplay of the Raman and higher-order dispersion effects", *Physical Review A*, vol. 92, no. 3, p. 033 851, 2015. DOI: 10.1103/PhysRevA.92.033851.

[130] C. Bao, L. Zhang, L. C. Kimerling, J. Michel, and C. Yang, "Soliton breathing induced by stimulated Raman scattering and self-steepening in octave-spanning Kerr frequency comb generation", *Optics Express*, vol. 23, no. 14, pp. 18 665–18 670, 2015. DOI: 10.1364/OE.23.018665.

[131] F. Leo, T. Hansson, I. Ricciardi, M. De Rosa, S. Coen, S. Wabnitz, and M. Erkintalo, "Walk-off-induced modulation instability, temporal pattern formation, and frequency comb generation in cavity-enhanced second-harmonic generation", *Physical Review Letters*, vol. 116, no. 3, p. 033 901, 2016. DOI: 10.1103/PhysRevLett.116.033901.

[132] ——, "Frequency-comb formation in doubly resonant second-harmonic generation", *Physical Review A*, vol. 93, no. 4, p. 043 831, 2016. DOI: 10.1103/PhysRevA.93.043831.

[133] X. Xue, F. Leo, Y. Xuan, J. A. Jaramillo-Villegas, P.-H. Wang, D. E. Leaird, M. Erkintalo, M. Qi, and A. M. Weiner, "Second-harmonic-assisted four-wave mixing in chip-based microresonator frequency comb generation", *Light: Science & Applications*, vol. 6, no. 4, e16253, 2017. DOI: 10.1038/lsa.2016.253.

[134] T. Kobatake, T. Kato, H. Itobe, Y. Nakagawa, and T. Tanabe, "Thermal effects on Kerr comb generation in a CaF_2 whispering-gallery-mode microcavity", *IEEE Photonics Journal*, vol. 8, no. 2, pp. 1–9, 2016. DOI: 10.1109/JPHOT.2016.2538965.

[135] Q. Li, T. C. Briles, D. A. Westly, T. E. Drake, J. R. Stone, B. R. Ilic, S. A. Diddams, S. B. Papp, and K. Srinivasan, "Stably accessing octave-spanning microresonator frequency combs in the soliton regime", *Optica*, vol. 4, no. 2, pp. 193–203, 2017. DOI: 10.1364/OPTICA.4.000193.

[136] M. Haelterman, S. Trillo, and S. Wabnitz, "Additive-modulation-instability ring laser in the normal dispersion regime of a fiber", *Optics Letters*, vol. 17, no. 10, pp. 745–747, 1992. DOI: 10.1364/OL.17.000745.

[137] C. Godey, I. V. Balakireva, A. Coillet, and Y. K. Chembo, "Stability analysis of the spatiotemporal Lugiato-Lefever model for Kerr optical frequency combs in the anomalous and normal dispersion regimes", *Physical Review A*, vol. 89, no. 6, p. 063 814, 2014. DOI: 10.1103/PhysRevA.89.063814.

[138] C. Godey, "A bifurcation analysis for the Lugiato-Lefever equation", *The European Physical Journal D*, vol. 71, no. 5, p. 131, 2017. DOI: 10.1140/epjd/e2017-80057-2.

[139] Y. Okawachi, M. R. E. Lamont, K. Luke, D. O. Carvalho, M. Yu, M. Lipson, and A. L. Gaeta, "Bandwidth shaping of microresonator-based

frequency combs via dispersion engineering", *Optics Letters*, vol. 39, no. 12, pp. 3535–3538, 2014. DOI: 10.1364/OL.39.003535.

[140] S.-W. Huang, H. Zhou, J. Yang, J. F. McMillan, A. Matsko, M. Yu, D.-L. Kwong, L. Maleki, and C. W. Wong, "Mode-locked ultrashort pulse generation from on-chip normal dispersion microresonators", *Physical Review Letters*, vol. 114, no. 5, p. 053 901, 2015. DOI: 10.1103/PhysRevLett.114.053901.

[141] Y. Liu, Y. Xuan, X. Xue, P.-H. Wang, S. Chen, A. J. Metcalf, J. Wang, D. E. Leaird, M. Qi, and A. M. Weiner, "Investigation of mode coupling in normal-dispersion silicon nitride microresonators for Kerr frequency comb generation", *Optica*, vol. 1, no. 3, pp. 137–144, 2014. DOI: 10.1364/OPTICA.1.000137.

[142] X. Xue, Y. Xuan, P. H. Wang, Y. Liu, D. E. Leaird, M. Qi, and A. M. Weiner, "Normal-dispersion microcombs enabled by controllable mode interactions", *Laser and Photonics Reviews*, vol. 9, no. 4, pp. L23–L28, 2015. DOI: 10.1002/lpor.201500107.

[143] G. D'Aguanno and C. R. Menyuk, "Nonlinear mode coupling in whispering-gallery-mode resonators", *Physical Review A*, vol. 93, no. 4, p. 043 820, 2016. DOI: 10.1103/PhysRevA.93.043820.

[144] ——, "Coupled Lugiato-Lefever equation for nonlinear frequency comb generation at an avoided crossing of a microresonator", *The European Physical Journal D*, vol. 71, no. 3, p. 74, 2017. DOI: 10.1140/epjd/e2017-70705-x.

[145] K. Ikeda, R. E. Saperstein, N. Alic, and Y. Fainman, "Thermal and Kerr nonlinear properties of plasma-deposited silicon nitride/ silicon dioxide waveguides", *Optics Express*, vol. 16, no. 17, pp. 12 987–12 994, 2008. DOI: 10.1364/OE.16.012987.

[146] T. Carmon, L. Yang, and K. J. Vahala, "Dynamical thermal behavior and thermal self-stability of microcavities", *Optics Express*, vol. 12, no. 20, pp. 4742–4750, 2004. DOI: 10.1364/OPEX.12.004742.

[147] A. Coillet, I. Balakireva, R. Henriet, K. Saleh, L. Larger, J. M. Dudley, C. R. Menyuk, and Y. K. Chembo, "Azimuthal Turing patterns, bright and dark cavity solitons in Kerr combs generated with whispering-gallery-mode resonators", *IEEE Photonics Journal*, vol. 5, no. 4, p. 6 100 409, 2013. DOI: 10.1109/JPHOT.2013.2277882.

[148] S. Coen and M. Erkintalo, "Universal scaling laws of Kerr frequency combs", *Optics Letters*, vol. 38, no. 11, pp. 1790–1792, 2013. DOI: 10.1364/OL.38.001790.

[149] T. Hansson, D. Modotto, and S. Wabnitz, "Dynamics of the modulational instability in microresonator frequency combs", *Physical Review A*, vol. 88, no. 2, p. 023 819, 2013. DOI: 10.1103/PhysRevA.88.023819.

[150] A. Coillet and Y. Chembo, "On the robustness of phase locking in Kerr optical frequency combs", *Optics Letters*, vol. 39, no. 6, pp. 1529–1532, 2014. DOI: 10.1364/OL.39.001529.

[151] A. M. Turing, "The chemical basis of morphogenesis", *Philosophical Transactions of the Royal Society B: Biological Sciences*, vol. 237, no. 641, pp. 37–72, 1952. DOI: 10.1098/rstb.1952.0012.

[152] P.-H. Wang, Y. Xuan, L. Fan, L. T. Varghese, J. Wang, Y. Liu, X. Xue, D. E. Leaird, M. Qi, and A. M. Weiner, "Drop-port study of microresonator frequency combs: Power transfer, spectra and time-domain characterization", *Optics Express*, vol. 21, no. 19, pp. 22 441–22 452, 2013. DOI: 10.1364/OE.22.012148.

[153] M. R. E. Lamont, Y. Okawachi, and A. L. Gaeta, "Route to stabilized ultrabroadband microresonator-based frequency combs", *Optics Letters*, vol. 38, no. 18, pp. 3478–3481, 2013. DOI: 10.1364/OL.38.003478.

[154] M. Erkintalo and S. Coen, "Coherence properties of Kerr frequency combs", *Optics Letters*, vol. 39, no. 2, pp. 283–286, 2014. DOI: 10.1364/OL.39.000283.

[155] J. A. Jaramillo-Villegas, X. X. Xue, P. H. Wang, D. E. Leaird, and A. M. Weiner, "Deterministic single soliton generation and compression in microring resonators avoiding the chaotic region", *Optics Express*, vol. 23, no. 8, pp. 9618–9626, 2015. DOI: 10.1364/oe.23.009618.

[156] K. Saha, Y. Okawachi, B. Shim, J. S. Levy, R. Salem, A. R. Johnson, M. A. Foster, M. R. E. Lamont, M. Lipson, and A. L. Gaeta, "Modelocking and femtosecond pulse generation in chip-based frequency combs", *Optics Express*, vol. 21, no. 1, pp. 1335–1343, 2013. DOI: 10.1364/OE.21.001335.

[157] V. Brasch, M. Geiselmann, M. H. P. Pfeiffer, and T. J. Kippenberg, "Bringing short-lived dissipative Kerr soliton states in microresonators into a steady state", *Optics Express*, vol. 24, no. 25, p. 29 312, 2016. DOI: 10.1364/OE.24.029312.

[158] H. Guo, M. Karpov, E. Lucas, A. Kordts, M. Pfeiffer, V. Brasch, G. Lihachev, V. Lobanov, M. Gorodetsky, and T. Kippenberg, "Universal dynamics and deterministic switching of dissipative Kerr solitons in optical microresonators", *Nature Physics*, vol. 13, no. 1, pp. 94–102, 2016. DOI: 10.1038/nphys3893.

[159] X. Yi, Q.-F. Yang, K. Youl, and K. Vahala, "Active capture and stabilization of temporal solitons in microresonators", *Optics Letters*, vol. 41, no. 9, pp. 2037–2040, 2016. DOI: 10.1364/OL.41.002037.

[160] C. Joshi, J. K. Jang, K. Luke, X. Ji, S. A. Miller, A. Klenner, Y. Okawachi, M. Lipson, and A. L. Gaeta, "Thermally controlled comb generation and soliton modelocking in microresonators", *Optics Letters*, vol. 41, no. 11, pp. 2565–2568, 2016. DOI: 10.1364/OL.41.002565.

[161] S. Wabnitz, "Suppression of interactions in a phase-locked soliton optical memory", *Optics Letters*, vol. 18, no. 8, pp. 601–603, 1993. DOI: 10.1364/OL.18.000601.

[162] I. V. Barashenkov and Y. S. Smirnov, "Existence and stability chart for the ac-driven, damped nonlinear Schrödinger solitons", *Physical Review E*, vol. 54, no. 5, pp. 5707–5725, 1996. DOI: 10.1103/PhysRevE.54.5707.

[163] X. Yi, Q.-F. Yang, K. Y. Yang, M.-G. Suh, and K. Vahala, "Soliton frequency comb at microwave rates in a high-Q silica microresonator", *Optica*, vol. 2, no. 12, pp. 1078–1085, 2015. DOI: 10.1364/OPTICA.2.001078.

[164] V. Brasch, E. Lucas, J. D. Jost, M. Geiselmann, and T. J. Kippenberg, "Self-referenced photonic chip soliton Kerr frequency comb", *Light: Science & Applications*, vol. 6, no. 1, e16202, 2017. DOI: 10.1038/lsa.2016.202.

[165] D. T. Spencer, T. Drake, T. C. Briles, J. Stone, L. C. Sinclair, C. Fredrick, Q. Li, D. Westly, B. R. Ilic, A. Bluestone, N. Volet, T. Komljenovic, L. Chang, S. H. Lee, D. Y. Oh, M.-G. Suh, K. Y. Yang, M. H. P. Pfeiffer, T. J. Kippenberg, E. Norberg, L. Theogarajan, K. Vahala, N. R. Newbury, K. Srinivasan, J. E. Bowers, S. A. Diddams, and S. B. Papp, "An integrated-photonics optical-frequency synthesizer", *arXiv preprint*, p. 1708.05228, 2017.

[166] P. Trocha, M. Karpov, D. Ganin, M. H. P. Pfeiffer, A. Kordts, S. Wolf, J. Krockenberger, P. Marin-Palomo, C. Weimann, S. Randel, W. Freude, T. J. Kippenberg, and C. Koos, "Ultrafast optical ranging using microresonator soliton frequency combs", *Science*, vol. 359, no. 6378, pp. 887–891, 2018. DOI: 10.1126/science.aao3924.

[167] M.-G. Suh and K. J. Vahala, "Soliton microcomb range measurement", *Science*, vol. 359, no. 6378, pp. 884–887, 2018. DOI: 10.1126/science.aao1968.

[168] C. Bao, Y. Xuan, J. A. Jaramillo-Villegas, D. E. Leaird, M. Qi, and A. M. Weiner, "Direct soliton generation in microresonators", *Optics Letters*, vol. 42, no. 13, pp. 2519–2522, 2017. DOI: 10.1364/OL.42.002519.

[169] F. Leo, S. Coen, P. Kockaert, S.-P. Gorza, P. Emplit, and M. Haelterman, "Temporal cavity solitons in one-dimensional Kerr media as bits in an all-optical buffer", *Nature Photonics*, vol. 4, no. 7, pp. 471–476, 2010. DOI: 10.1038/nphoton.2010.120.

[170] D. C. Cole, E. S. Lamb, P. Del'Haye, S. A. Diddams, and S. B. Papp, "Soliton crystals in Kerr resonators", *Nature Photonics*, vol. 11, no. 10, pp. 671–676, 2017. DOI: 10.1038/s41566-017-0009-z.

[171] W. Liang, A. a. Savchenkov, V. S. Ilchenko, D. Eliyahu, D. Seidel, A. B. Matsko, and L. Maleki, "Generation of a coherent near-infrared Kerr frequency comb in a monolithic microresonator with normal GVD", *Optics Letters*, vol. 39, no. 10, pp. 2920–2923, 2014. DOI: 10.1364/OL.39.002920.

[172] C. Wang, C. Bao, Y. Xuan, K. Han, D. Leaird, M. Qi, and A. Weiner, "Normal dispersion high conversion efficiency Kerr comb with 50 GHz repetition rate", in *Conference on Lasers and Electro-Optics*, vol. 11, San Jose, USA: OSA, 2017, SW4N.5. DOI: 10.1364/CLEO_SI.2017.SW4N.5.

[173] V. Lobanov, G. Lihachev, T. J. Kippenberg, and M. Gorodetsky, "Frequency combs and platicons in optical microresonators with normal GVD", *Optics Express*, vol. 23, no. 6, pp. 7713–7721, 2015. DOI: 10.1364/OE.23.007713.

[174] V. E. Lobanov, A. V. Cherenkov, A. E. Shitikov, I. A. Bilenko, and M. L. Gorodetsky, "Dynamics of platicons due to third-order dispersion", *The European Physical Journal D*, vol. 71, no. 7, p. 185, 2017. DOI: 10.1140/epjd/e2017-80148-0.

[175] N. N. Rozanov, V. E. Semenov, and G. V. Khodova, "Transverse structure of a field in nonlinear bistable interferometers. i. switching waves and steady-state profiles", *Soviet Journal of Quantum Electronics*, vol. 12, no. 2, pp. 193–197, 1982. DOI: 10.1070/QE1982v012n02ABEH005474.

[176] S. Coen, M. Tlidi, P. Emplit, and M. Haelterman, "Convection versus dispersion in optical bistability", *Physical Review Letters*, vol. 83, no. 12, pp. 2328–2331, 1999. DOI: 10.1103/PhysRevLett.83.2328.

[177] P. Parra-Rivas, D. Gomila, E. Knobloch, S. Coen, and L. Gelens, "Origin and stability of dark pulse Kerr combs in normal dispersion resonators", *Optics Letters*, vol. 41, no. 11, pp. 2402–2405, 2016. DOI: 10.1364/OL.41.002402.

[178] P. Parra-Rivas, E. Knobloch, D. Gomila, and L. Gelens, "Dark solitons in the Lugiato-Lefever equation with normal dispersion", *Physical Review A*, vol. 93, no. 6, p. 063 839, 2016. DOI: 10.1103/PhysRevA.93.063839.

[179] P. Parra-Rivas, D. Gomila, and L. Gelens, "Coexistence of stable dark- and bright-soliton Kerr combs in normal-dispersion resonators", *Physical Review A*, vol. 95, no. 5, p. 053 863, 2017. DOI: 10.1103/PhysRevA.95.053863.

[180] S. A. Miller, Y. Okawachi, S. Ramelow, K. Luke, A. Dutt, A. Farsi, A. L. Gaeta, and M. Lipson, "Tunable frequency combs based on dual microring resonators", *Optics Express*, vol. 23, no. 16, pp. 21 527–21 540, 2015. DOI: 10.1364/OE.23.021527.

[181] M.-G. Suh and K. Vahala, "Gigahertz-repetition-rate soliton microcombs", *Optica*, vol. 5, no. 1, pp. 65–66, 2018. DOI: 10.1364/OPTICA.5.000065.

[182] X. Yi, Q.-F. Yang, X. Zhang, K. Y. Yang, X. Li, and K. Vahala, "Single-mode dispersive waves and soliton microcomb dynamics", *Nature Communications*, vol. 8, p. 14 869, 2017. DOI: 10.1038/ncomms14869.

[183] I. Fatadin, S. J. Savory, and D. Ives, "Compensation of quadrature imbalance in an optical QPSK coherent receiver", *IEEE Photonics Technology Letters*, vol. 20, no. 20, pp. 1733–1735, 2008. DOI: 10.1109/LPT.2008.2004630.

[184] M. Selmi, Y. Jaouën, and P. Ciblat, "Accurate digital frequency offset estimator for coherent PolMux QAM transmission systems", in *European Conference on Optical Communications (ECOC)*, 2009, P3.08.

[185] I. Fatadin, D. Ives, and S. Savory, "Blind equalization and carrier phase recovery in a 16-QAM optical coherent system", *Journal of Lightwave Technology*, vol. 27, no. 15, pp. 3042–3049, 2009. DOI: 10.1109/JLT.2009.2021961.

Appendices

Appendix A — Offline coherent receiver DSP

Digital signal processing is required to recover the transmitted data from a received signal at the end of an optical fiber link. The flowchart in figure 6.1 describes the code of the DSP used in Paper D. The signal recorded in a real-time oscilloscope needs to be processed in several steps:

1. Impairments originating from the receiver need to be handled first. This starts by compensating for relative delays caused by varying electrical lengths of cables and waveguides. Second, any remaining phase offsets and power differences in the varying arms need to be compensated for. This can be done using Gram-Schmidt orthogonalization [183]. Finally, the received signal is typically resampled to an integer number samples per symbol, two in the case of Paper D.

2. Static link effects known in advance can now be handled. In our case this meant compensating for the fiber's chromatic dispersion.

3. Dynamic link (and receiver) effects need to be handled by a multi-tap adaptive equalizer. Figure 6.2 (a) describes its basic operation. By looping over the signal, an equalizers taps can dynamically handle polarization-mode dispersion as well as residual chromatic dispersion. To train the equalizer taps in the laboratory scenario, they were looped over the signal several times. This section of the DSP also includes frequency offset estimation between the local oscillator and the transmitter laser [184] as well as tracking of the carrier's phase noise as shown in figure 6.2 (b) [185].

4. The DSP now handles the remaining impairments from the transmitter. In practice, we perform a second Gram-Schmidt orthogonalization.

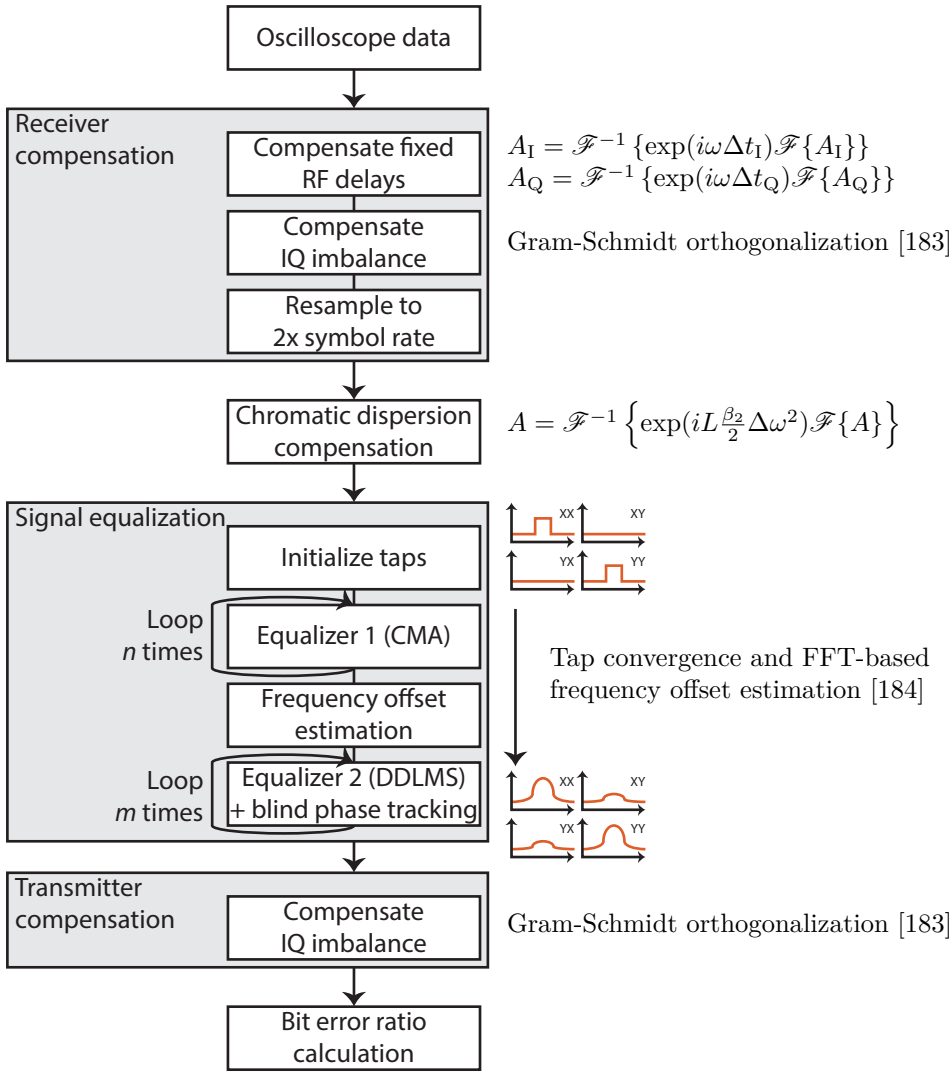

Figure 6.1. Flow chart showing the main components of a DSP algorithm for decoding M-ary QAM.

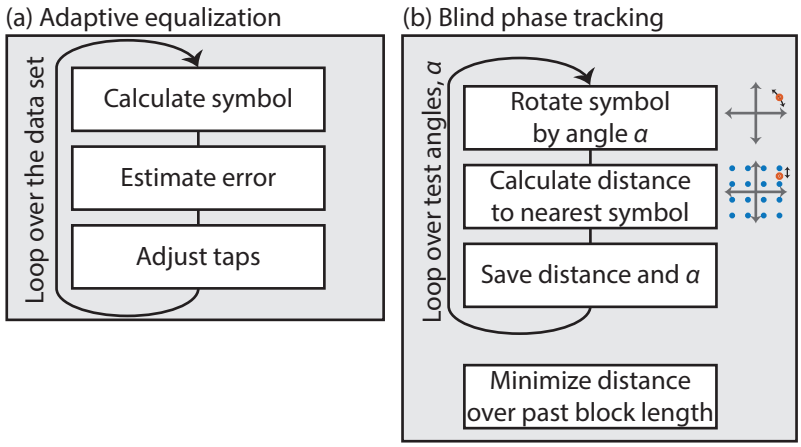

Figure 6.2. (a) The adaptive equalizer transverses over the signal. For each symbol it calculates an error metric and adjusts its taps to minimize it. In the CMA equalizer case, the error metric is the difference between the symbol power and a prescribed target reference power. In the DDLMS case, the error metric is the distance between the decoded symbol and the nearest available constellation point. (b) In the DDLMS case, the phase of the signal has to be tracked before the error can be estimated. Blind phase tracking involves testing a set of phases and assuming the one that gives the lowest mean square error over a block length [185].

5. Finally, the symbols extracted from the final equalizer loop are decoded to bits (typically using Grey coding). In the laboratory scenario we now compare the results to the known transmitted bit sequence yielding a final system bit error ratio.

Appendix B — Microresonator simulation

The simulations in Paper D were performed using the Ikeda map approach to allow coupling in random noise after each roundtrip as well as during propagation [120–122]. To reproducibly converge to a dark pulse comb, the intracavity field was initialized with a square wave according to [91]. Figure 6.3 (a) contains a flow chart of the method. The propagation along the resonator was done using the standard split-step technique [33] with figure 6.3 (b) showing the steps.

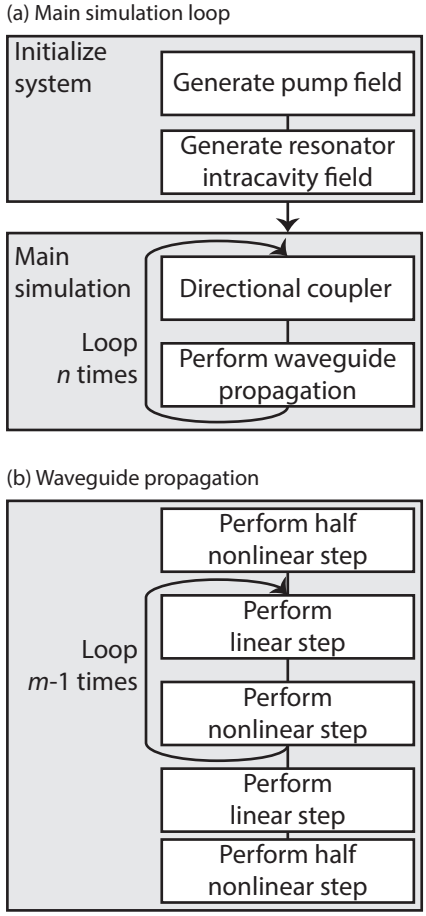

$$A_{\mathrm{pump}} = \mathscr{F}^{-1}\left\{\sqrt{P_{\mathrm{in}}} + \sqrt{\tfrac{\hbar\omega}{2}}\exp(i\phi_{\mathrm{rand}})\right\}$$

Start A_{in} with a square wave with 50% duty cycle. The top and bottom levels are given by the bistability curves [91].

Couple light in and out of the resonator:

$$A_{\mathrm{out}} = A_{\mathrm{pump}}\sqrt{1-\theta} - A_{\mathrm{in}}\exp(i\phi_0)\sqrt{\theta}$$
$$A_{\mathrm{in}} = A_{\mathrm{in}}\exp(i\phi_0)\sqrt{1-\theta} + A_{\mathrm{pump}}\sqrt{\theta}$$

Perform linear step:

$$A_{\mathrm{in}} = \mathscr{F}^{-1}\{\exp(i\beta\Delta L)\exp\left(-\tfrac{\alpha L}{2}\right)\mathscr{F}\{A_{\mathrm{in}}\} + \sqrt{1-\exp(-\alpha\Delta L)}\sqrt{\hbar\omega/2}\exp(i\phi_{\mathrm{rand}})\}$$

Perform nonlinear step:

$$A_{\mathrm{in}} = A_{\mathrm{in}}\exp\left(i|A_{\mathrm{in}}|^2\gamma\Delta L\right)$$

Figure 6.3. (a) Flow chart showing the main steps in the Ikeda map simulation. The main simulation loop typically runs $n > 2^{14}$ roundtrips until the system converges. (b) The waveguide propagation is performed according to the standard split-step method [33]. To keep noise levels realistic also in the presence of high losses, each loss step (in the linear part) also couples in quantum noise at the appropriate level.

Appendix C — Microresonator stage

To enable pumping and stabilizing the microresonator comb operation, the stage shown in figure 6.4 was used. A continuously tunable pump laser (Toptica CTL 1550) and a high-power amplifier was used to generate the pumping

laser light. Using an optical bandpass filter centered around the pumping wavelength of 1540 nm (in practice a WDM-coupler selecting ITU grid channel 47), we could minimize the amount of excess ASE noise entering the resonator. The chip itself was placed on a piezo-controlled positioning stage. The stage contains a vacuum pump to minimize movement of the chip over long timescales as well as a temperature controller stabilizing the stage temperature. See figure 6.5 for a labelled photograph. Following the chip, an OSA (Ando AQ6317B) was used to monitor the optical spectrum. To allow locking of the comb state, one of the newly generated comb lines was additionally filtered out and measured in a photodiode. The low-frequency (< 10 kHz) component of the power drift was fed back to the laser providing a locking point. Any mid and high-frequency noise measured by the photodiode was measured in an electrical ESA (Rigol DSA815) allowing visual verification of the low-noise comb state.

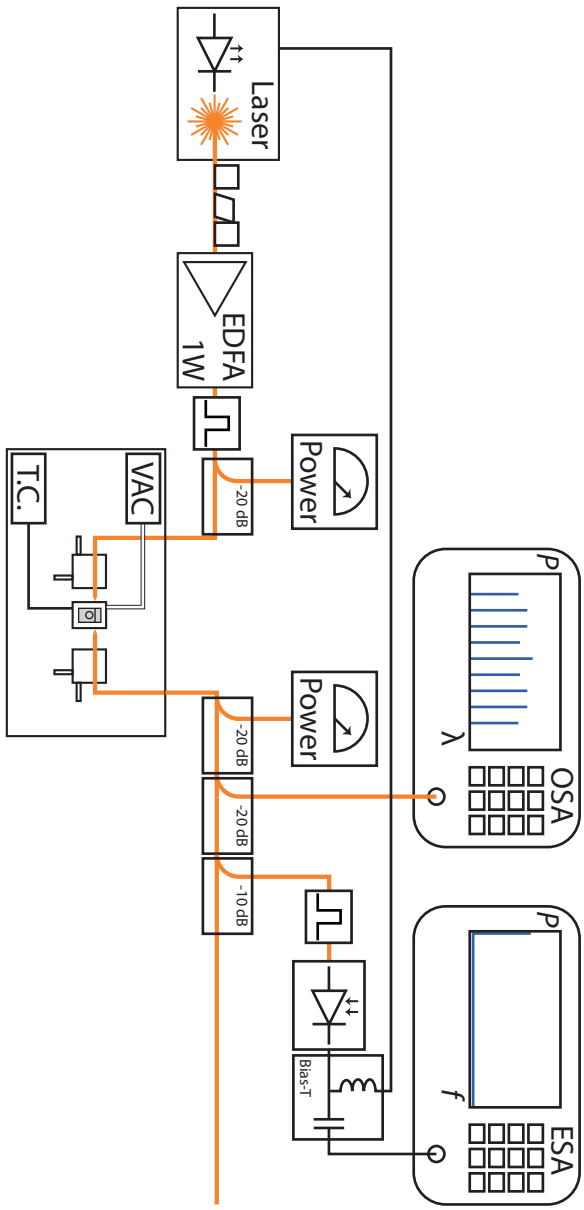

Figure 6.4. Microresonator stage setup with all the required components.

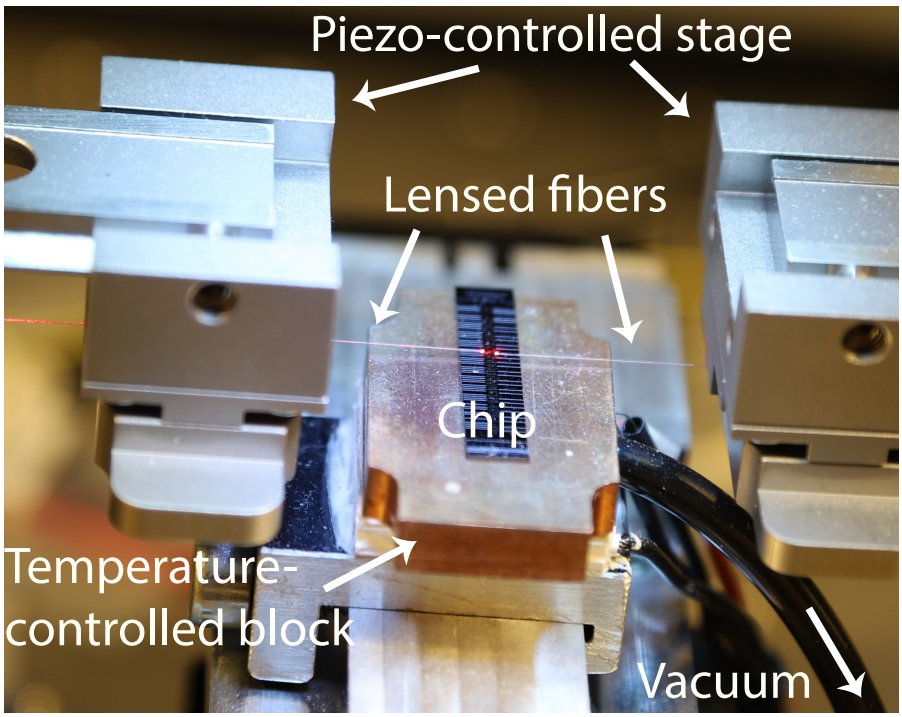

Figure 6.5. Labelled photo of the microresonator mounting stage.